Length Scale of the Finite-Amplitude Meanders of Shelfbreak Fronts

WEIFENG G. ZHANG

Applied Ocean Physics and Engineering Department, Woods Hole Oceanographic Institution, Woods Hole, Massachusetts

GLEN G. GAWARKIEWICZ

Physical Oceanography Department, Woods Hole Oceanographic Institution, Woods Hole, Massachusetts

ABSTRACT

Through combining analytical arguments and numerical models, this study investigates the finite-amplitude meanders of shelfbreak fronts characterized by sloping isopycnals outcropping at both the surface and the shelfbreak bottom. The objective is to provide a formula for the meander length scale that can explain observed frontal length scale variability and also be verified with observations. Considering the frontal instability to be a mixture of barotropic and baroclinic instability, the derived along-shelf meander length scale formula is $[b_1/(1 + a_1S^{1/2})]NH/f$, where N is the buoyancy frequency; H is the depth of the front; f is the Coriolis parameter; S is the Burger number measuring the ratio of energy conversion associated with barotropic and baroclinic instability; and a_1 and b_1 are empirical constants. Initial growth rate of the frontal instability is formulated as $[b_2(1 + a_1S^{1/2})/(1 + a_2\alpha S^{1/2})]NH/L$, where α is the bottom slope at the foot of the front, and a_2 and b_2 are empirical constants. The formulas are verified using numerical sensitivity simulations, and fitting of the simulated and formulated results gives $a_1 = 2.69$, $b_1 = 14.65$, $a_2 = 5.1 \times 10^3$, and $b_2 = 6.2 \times 10^{-2}$. The numerical simulations also show development of fast-growing frontal symmetric instability when the minimum initial potential vorticity is negative. Although frontal symmetric instability leads to faster development of barotropic and baroclinic instability at later times, it does not significantly influence the meander length scale. The derived meander length scale provides a framework for future studies of the influences of external forces on shelfbreak frontal circulation and cross-frontal exchange.

1. Introduction

Shelfbreak fronts exist on many continental shelves, such as the Mid-Atlantic Bight (MAB) shelf (Voorhis et al. 1976), the east Bering Sea shelf (Kinder and Coachman 1978), the Celtic Sea shelf (Pingree 1979), and the east Greenland shelf (Brearley et al. 2012). Shelfbreak frontal zones often hold higher levels of mechanical energy than the neighboring regions, as frontal horizontal density gradients store potential energy and frontal currents contain high levels of kinetic energy. This makes shelfbreak fronts susceptible to perturbation growth that tends to redistribute the frontal energy through introducing spatiotemporal variability to the frontal circulation while converting energy from mean to fluctuation states.

In the MAB, the persistent shelfbreak front (Fig. 1) separates the lower-density, cooler, fresher water on the shelf from the higher-density, warmer, more saline water offshore (Fratantoni and Pickart 2003; Houghton et al. 1988; Linder and Gawarkiewicz 1998). It is a retrograde shelfbreak front (Lozier and Reed 2005) as the frontal isopycnals shoal offshore opposing the slope of the seafloor. Associated with the shelfbreak front is an along-shelf jet that can at times reach a speed of $0.5\,\mathrm{m\,s^{-1}}$ (Gawarkiewicz et al. 2001). This type of density front is subject to instability (Barth 1994; Brink 2012; Gawarkiewicz 1991; Lozier and Reed 2005), which can grow into finite-amplitude frontal meanders (Cenedese and Linden 2002; Garvine et al. 1988) (e.g., Figs. 2a,b). One important aspect of the frontal meanders is the along-shelf length scale, which can potentially affect frontal exchange processes that transport

Corresponding author address: Weifeng G. Zhang, Applied Ocean Physics and Engineering Department, Woods Hole Oceanographic Institution, 266 Woods Hole Road, Woods Hole, MA 02543.
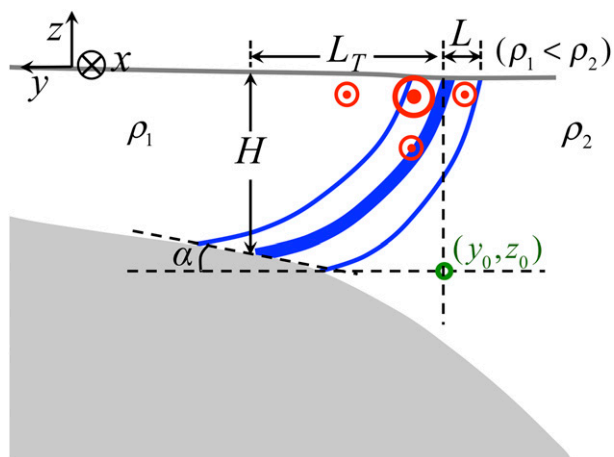E-mail: wzhang@whoi.edu

FIG. 1. Schematic of the Mid-Atlantic Bight retrograde shelfbreak front with isopycnal slope opposing the bottom slope. The solid gray line depicts the undisturbed sea level; the blue lines depict the frontal isopycnals with the thick one representing the central isopycnal; the red dot circles depict the along-shelf flow, with the size indicating relative strength; the green circle indicates the location of (y_0, z_0) used in (21). The terms H and L_T indicate the vertical and cross-shelf extent of the central isopycnal, respectively; L is the half-width of the front; and α is the bottom slope at the foot of the front. Here, H and L are also the vertical and horizontal length scales of the density variation, respectively, corresponding to those in the theoretical scalings. The dimensions are not to scale.

heat, salt, and biogeochemical substances across the shelf break.

From repeated hydrographic surveys, Gawarkiewicz et al. (2004) reported frontal variability at the MAB shelf break dominated by a westward-moving meander with a wavelength of 40 km, slightly larger than a previously observed 33-km wavelength (Garvine et al. 1988). Recent subsurface glider measurements in the same region show along-shelf periodicity with a wavelength of 40–50 km (Todd et al. 2013). These observed wavelength variations possibly indicate variability in the frontal meander length scale at the MAB shelf break as at shelfbreak regions elsewhere (e.g., Pingree 1979). Variability in the meander length scale can be quantified more directly from satellite measurements (e.g., Fig. 2). Frontal wavelength in the shelfbreak region of 71°–70°E is ~40 km on 13 April 2014 and ~60 km on 17 April 2009; frontal wavelength on 17 April 2009 in a nearby shelfbreak region of 73°–72°E is ~25 km. It is intriguing to know what causes these spatiotemporal variations of the frontal meander length scale, a question that remains to be answered despite the aforementioned numerous studies of the MAB shelfbreak front.

This work aims to understand the mechanism that determines the along-shelf length scale of the finite-amplitude meanders of a wintertime shelfbreak front and to provide a formula for the length scale that can be

verified in future observational studies. We emphasize the finite-amplitude behavior here because real ocean measurements, in situ or remote, can only capture finite-amplitude frontal variations. Furthermore, as indicated by the aforementioned examples, finite-amplitude frontal meanders are a common occurrence at shelfbreak regions, including the MAB shelfbreak region. Formulation of the length scale will be based on theories of linear barotropic and baroclinic instability as well as physical characteristics of the shelfbreak front. To gain additional insight into the frontal dynamics, we also derive a formula for the initial growth rate of the frontal instability.

The formulas will be validated against numerical models that simulate the spindown process of initially straight, baroclinically unstable shelfbreak fronts. The simulations are equivalent to the wintertime situations in the real ocean that external forcings, for example, windstorms, homogenize waters on one or both sides of the shelf break, leaving a relative straight surface outcropping density front. Subject to instability, both simulated and real ocean fronts (e.g., Figs. 2a,b) develop into meanders and shed eddies propagating onshore or offshore. The simulated frontal spindown process then proceeds into the stage of a complete breakdown of the fronts into eddies. This last step generally does not happen in the real ocean owing to the supply of buoyancy to the shelf water by a number of processes, for example, upstream advection, coastal freshwater input, and surface heat flux, that sustain the cross-front density contrast (Chapman and Lentz 1994). Absence of these buoyancy sources in the model results in the unrealistic breakdown of the fronts after full development of the meanders. We thus examine the length scale of the modeled frontal variability only at the meander stage to achieve applicability in the real ocean.

The paper is organized as follows: Section 2 synthesizes some theoretical results of linear instability. Section 3 describes the setup of the numerical model. Section 4 presents the model results, the formulation procedure, and verification of the formulas. The findings are summarized in section 5.

2. Background on linear instability

Here, we synthesize aspects of baroclinic, barotropic, and symmetric instability that are relevant to this study and introduce the corresponding scaling formulas in the context of shelfbreak fronts. Although these formulas are for the lowest-order development of small-amplitude perturbations, they provide the necessary background for the formulation of length scale and growth rate of the shelfbreak frontal instability in section 4b.
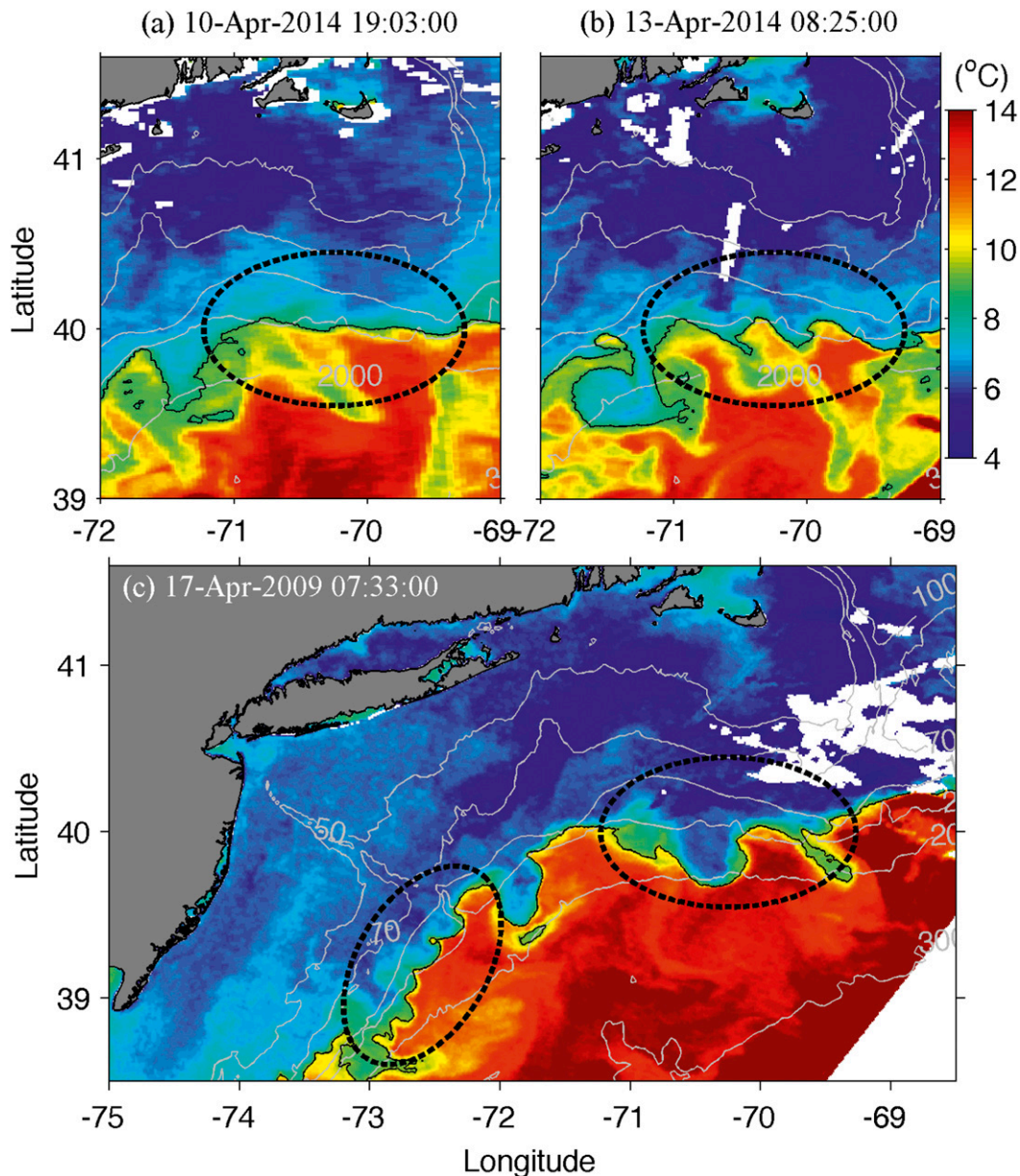
FIG. 2. Sea surface temperature in the northern Mid-Atlantic Bight on (a) 10 Apr 2014, (b) 13 Apr 2014, and (c) 17 Apr 2009. The gray lines are isobath contours; the thin black lines indicate the surface outcrop of the shelfbreak front; and the dashed ellipses highlight the frontal regions mentioned in the text. White patches are missing data due to cloud cover.

a. Baroclinic instability

Pedlosky (1987) considered a geostrophically balanced, continuously stratified, inviscid zonal flow that is bounded in the meridional direction by rigid walls at $\hat{y} = \pm 1$ ($y = y_1$ in the south and $y = y_2$ in the north) and has $O(1)$ Burger number:

$$S = \left(\frac{NH}{fL}\right)^2. \tag{1}$$

The nondimensional zonal-mean velocity $\hat{U} = \hat{U}(\hat{y}, \hat{z})$ satisfies the thermal wind relation:

$$\frac{\partial \hat{U}}{\partial \hat{z}} = -\frac{\partial \widehat{\overline{\rho}}}{\partial \hat{y}}. \tag{2}$$

Here, variables with a hat are nondimensional; $\widehat{\overline{\rho}}$ is the nondimensional along-stream mean potential density; $N = [-(g/\rho_0)\partial\rho/\partial z]^{1/2}$ is the buoyancy frequency; H and

L are the vertical and horizontal scales of the density variation, respectively; ρ is the dimensional potential density; ρ_0 is the dimensional reference density; and g is the gravitational acceleration (see the appendix for the meanings of all dimensional notations). For linear instability caused by small-amplitude quasigeostrophic perturbations, Pedlosky (1987) obtained the perturbation energy growth rate:

$$\frac{\partial \hat{E}'}{\partial \hat{t}} = -\int_{-1}^{0}\int_{-1}^{1}\hat{\rho}_0 \left[\overline{\hat{v}'\hat{u}'}\frac{\partial \hat{U}}{\partial \hat{y}} + \frac{\overline{\hat{v}'\hat{\rho}'}}{S}\frac{\partial \widehat{\overline{\rho}}}{\partial \hat{y}}\right] d\hat{y}\, d\hat{z}. \quad (3)$$

Here, $\hat{E}'$ is nondimensional total perturbation energy; $\hat{u}' = \hat{u} - \hat{U}$ and $\hat{v}' = \hat{v}$ are nondimensional perturbation velocity in zonal and meridional directions, respectively; $\hat{u}$ and $\hat{v}$ are corresponding nondimensional total velocity; $\hat{\rho}' = \hat{\rho} - \widehat{\overline{\rho}}$, $\hat{\rho}$, and $\hat{\rho}_0$ are nondimensional perturbation, total, and reference potential density, respectively; and the overbar in this work indicates the along-stream (along shelf) average.

In (3), $-\int_{-1}^{0}\int_{-1}^{1}\hat{\rho}_0\overline{\hat{v}'\hat{u}'}(\partial \hat{U}/\partial \hat{y})\,d\hat{y}\,d\hat{z} = \hat{C}_{bt}$ represents perturbation growth caused by horizontal Reynolds stress through barotropic instability converting mean kinetic energy (MKE) to perturbation energy; $-\int_{-1}^{0}\int_{-1}^{1}\hat{\rho}_0(\overline{\hat{v}'\hat{\rho}'}/S)(\partial \widehat{\overline{\rho}}/\partial \hat{y})\,d\hat{y}\,d\hat{z} = \hat{C}_{bc}$ represents perturbation growth caused by horizontal buoyancy flux through baroclinic instability converting available potential energy (APE) to perturbation energy. Their ratio, that is, the ratio of energy conversion associated with barotropic and baroclinic instability, scales as

$$\frac{\hat{C}_{bt}}{\hat{C}_{bc}} = \frac{C_{bt}}{C_{bc}} = \left(\frac{NH}{fL}\right)^2 = S. \quad (4)$$

The dimensional energy conversion rates are $C_{bt} = -\int_{-h}^{0}\int_{y_1}^{y_2}\rho_0\overline{v'u'}(\partial U/\partial y)\,dy\,dz$ and $C_{bc} = -\int_{-h}^{0}\int_{y_1}^{y_2}(g/\rho_0)$ $(\overline{v'\rho'})(\partial\overline{\rho}/\partial y)/(\partial\overline{\rho}/\partial z)\,dy\,dz$, where h is the water depth.

Assuming the effect of the perturbation on the mean flow is merely to redistribute the zonal momentum spatially, Pedlosky (1987) obtained

$$\frac{\partial \hat{E}'}{\partial \hat{t}} = \int_{-1}^{0}\int_{-1}^{1}\frac{\hat{\rho}_0\hat{U}}{2}\frac{\partial\hat{\Pi}}{\partial\hat{y}}\frac{\partial\overline{\hat{\eta}^2}}{\partial\hat{t}}\,d\hat{y}\,d\hat{z}$$
$$- \int_{-1}^{1}\left[\frac{\hat{\rho}_0\hat{U}}{2}\left(\frac{1}{S}\frac{\partial\hat{U}}{\partial\hat{z}} - \frac{\partial\hat{h}_B}{\partial\hat{y}}\right)\frac{\partial\overline{\hat{\eta}^2}}{\partial\hat{t}}\right]_{\hat{z}=-1}d\hat{y}$$
$$+ \int_{-1}^{1}\left[\frac{\hat{\rho}_0\hat{U}}{2S}\frac{\partial\hat{U}}{\partial\hat{z}}\frac{\partial\overline{\hat{\eta}^2}}{\partial\hat{t}}\right]_{\hat{z}=0}d\hat{y}. \quad (5)$$

Here, $\hat{\Pi}$ is nondimensional potential vorticity; $\hat{\eta}(x, y, z, t)$ is the nondimensional meridional displacement of fluid elements; and $\hat{h}_B$ (>0) is the nondimensional elevation of

the bottom above a reference level. The middle term on the right-hand side of (5) represents the bottom influence, and the factor within can be translated back into the dimensional space as

$$\left(\frac{1}{S}\frac{\partial\hat{U}}{\partial\hat{z}} - \frac{\partial\hat{h}_B}{\partial\hat{y}}\right)_{\hat{z}=-1} = \frac{L}{RoH}\left(\frac{\partial z}{\partial y}\bigg|_{\rho} - \frac{\partial h_B}{\partial y}\right)_{z=-D}$$
$$= \frac{L}{RoH}(\gamma - \alpha). \quad (6)$$

Here, $Ro = U/(fL)$ is the Rossby number with U being the dimensional zonal velocity; α and γ are the bottom slope and the isopycnal slope on the bottom, respectively. For a retrograde shelfbreak front (isopycnal slope opposes the bottom slope), $\alpha > 0$ and $\hat{U} < 0$ (Fig. 1), or $\alpha < 0$ and $\hat{U} > 0$. In a growing disturbance, $\partial\overline{\hat{\eta}^2}/\partial\hat{t} > 0$. Thus, (6) indicates that a sloping bottom suppresses the perturbation growth.

This effect of bottom slope is consistent with the finding of Blumsack and Gierasch (1972) on the quasigeostrophic baroclinic instability [$Ro \ll 1$ and $S \sim O(1)$] of a laterally unbounded flow of evenly spaced sloping isopycnals. It seemingly contradicts Lozier and Reed's (2005) claim that bottom slope enhances the instability of a retrograde shelfbreak front. However, Lozier and Reed's analysis was based on altering shelfbreak topography that modifies not only the bottom slope but also horizontal and vertical extents of the front. As will be demonstrated here, these frontal dimensions also have profound influences on the instability growth, which may explain the apparent discrepancy.

For a quasigeostrophic inviscid zonal flow on an f plane with uniformly tilted isopycnals over a flat bottom, Gill (1982) obtained the maximum perturbation growth rate of linear baroclinic instability:

$$\sigma_{bc} = 0.3098(f/N)|dU/dz|, \quad (7)$$

when the cross-stream wavenumber $m_{bc} = 0$ (cross-stream uniform perturbation in a laterally unbounded flow) and

$$Nk_{bc}H/2 = 0.8031f. \quad (8)$$

Here, k_{bc} is the along-stream (equivalent to along shelf in this study) wavenumber and H is the depth of the baroclinic flow. The corresponding along-stream length scale of baroclinic instability is

$$\lambda_{bc} = 2\pi/k_{bc} \approx (\pi/0.8031)NH/f. \quad (9)$$

Any variation in the cross-stream direction (as in the case of shelfbreak fronts) would cause $m_{bc} \neq 0$ and then λ_{bc} to be greater than (9) (Gill 1982). Note that the

baroclinic Rossby radius of deformation that determines the length scale of quasigeostrophic flow features, for example, mesoscale eddies (Charney and Flierl 1981), has the same scale of NH/f (Gill 1982).

b. Barotropic instability

The limited cross-shelf extent of the shelfbreak front also causes the geostrophic along-shelf flow to gradually weaken and eventually disappear away from the shelf break (Fig. 1). The associated velocity shear in the cross-shelf direction allows barotropic instability to occur, converting MKE to perturbation energy. Considering a quasigeostrophic, inviscid, zonal barotropic flow on an f plane with constant meridional shear $U = y \, dU/dy$, Gill (1982) obtained the maximum perturbation growth rate of the barotropic instability:

$$\sigma_{\text{bt}} = 0.2012 |dU/dy|. \quad (10)$$

The associated along-stream wavenumber is

$$k_{\text{bt}} = 0.7968/L_s, \quad (11)$$

where L_s is the shear zone width.

c. Symmetric instability

For a geostrophically balanced, inviscid, basic-state baroclinic flow on an f plane, ageostrophic symmetric instability occurs when (Allen and Newberger 1998; Brink and Cherian 2013; Haine and Marshall 1998; Thomas et al. 2013)

$$\Pi f < 0. \quad (12)$$

Here,

$$\Pi = \frac{1}{\rho_0} \left[-\frac{\partial \rho}{\partial z} \left(f - \frac{\partial u}{\partial y} + \frac{\partial v}{\partial x} \right) + \frac{\partial \rho}{\partial x} \frac{\partial v}{\partial z} - \frac{\partial \rho}{\partial y} \frac{\partial u}{\partial z} \right] \quad (13)$$

is the potential vorticity. The symmetric instability converts MKE to perturbation energy through developing slantwise convection in cross-stream recirculation cells (Stone 1966). One characteristic of symmetric instability is that the associated variability is mainly in the cross-stream and vertical directions, and the recirculation cells expand nearly uniformly along stream, that is, the along-stream wavenumber $k_{\text{si}} \approx 0$. For baroclinic flows of the Richardson number Ri < 0.95, symmetric instability develops faster than baroclinic instability (Stone 1966) and often leads to finite-amplitude baroclinic instability at later times (Boccaletti et al. 2007; Haine and Marshall 1998). Here, the Richardson number is defined as

$$\text{Ri} = \frac{N^2 H^2}{U^2}. \quad (14)$$

For a baroclinic flow unbounded in the cross-stream direction, Stone (1966) estimated the growth rate of symmetric instability:

$$\sigma_{\text{si}} = f \left(\frac{1}{\text{Ri}} - 1 \right)^{1/2}. \quad (15)$$

3. Model setup

The Regional Ocean Modeling System (Shchepetkin and McWilliams 2008) is used for simulating the frontal instability. The model is set up in Cartesian coordinates with the positive y direction pointing onshore (northward), positive x along shelf (eastward), and positive z pointing upward (Fig. 1), consistent with the orientation of the northern MAB shelf. A rectangular domain is used with edge lengths of $L_x = 480.5$ km and $L_y = 479$ km in the x and y directions, respectively, and in the y direction it extends from the coastal northern boundary at $y = 0$ to the offshore southern boundary at $y = -L_y$. The semirealistic model bathymetry is uniform in the x direction, and the cross-shelf depth is given by

$$h = \max \left(0, h_f \frac{y_p + l_f - y}{y_p + l_f} \right) + h_{p1} \tanh \frac{y - y_p}{l_p} - h_{p2}. \quad (16)$$

Here, the shelf width scale $l_f = 41$ km; the y coordinate of the center of the slope $y_p = -170.5$ km; the cross-shelf scale of the slope $l_p = 16.5$ km; the shelf depth scale $h_f = 65$ m; and the slope vertical scales $h_{p1} = 465$ m and $h_{p2} = 540$ m. The bathymetry in (16) starts from -10 m on the coast, deepens offshore at a constant rate of 0.5×10^{-3} on the shelf, and then transitions to a hyperbolic tangent shape in the slope sea. The bottom slope at the foot of the front (Fig. 1) is $\alpha = 1.7 \times 10^{-3}$. The 100-m isobath is located at $y = -140.7$ km. Values of the parameters are chosen to represent the northern MAB shelf and slope topography and to limit the maximum depth at 1005 m to maintain the model's vertical resolution in the deep sea. The inshore part of the model domain with width $L_{y0} = 323$ km (-323 km $\leq y \leq 0$ km) is the study area with a horizontal resolution of ~ 500 m. The remaining 156-km-wide deep sea region is a sponge layer for preventing wave reflection. Note that the shelf break is about 185 km away from the interior edge of the sponge layer, which gives ample space for the frontal instability to evolve. There are 60 stretched vertical sigma layers with enhanced resolution near the surface and bottom.

The model solves the Boussinesq hydrostatic equations of motion:

$$\frac{\partial u}{\partial t} + \mathbf{u} \cdot \nabla u - f v = -g\frac{\partial \xi}{\partial x} - \frac{gz}{\rho_0}\frac{\partial \rho}{\partial x} + \frac{\partial}{\partial z}\left(\kappa\frac{\partial u}{\partial z}\right), \qquad (17)$$

$$\frac{\partial v}{\partial t} + \mathbf{u} \cdot \nabla v + f u = -g\frac{\partial \xi}{\partial y} - \frac{gz}{\rho_0}\frac{\partial \rho}{\partial y} + \frac{\partial}{\partial z}\left(\kappa\frac{\partial v}{\partial z}\right), \qquad (18)$$

$$\nabla \cdot \mathbf{u} = 0, \quad \text{and} \qquad (19)$$

$$\frac{\partial \rho}{\partial t} + \nabla \cdot (\rho\mathbf{u}) = \frac{\partial}{\partial z}\left(\kappa_\theta\frac{\partial \rho}{\partial z}\right), \qquad (20)$$

with the boundary conditions of $\partial u/\partial z = 0$, $\partial v/\partial z = 0$, and $\partial \rho/\partial z = 0$ on the free surface ($z = \xi$) and $\kappa(\partial u/\partial z) = C_d|\mathbf{u}_{bh}|u_b$, $\kappa(\partial v/\partial z) = C_d|\mathbf{u}_{bh}|v_b$, and $\partial \rho/\partial z = 0$ on the bottom ($z = h$). Here, $\mathbf{u} = (u, v, w)$; w is vertical velocity; ξ is sea surface height; κ and κ_θ are vertical turbulence viscosity and diffusivity, respectively; C_d is the quadratic bottom drag coefficient; u_b and v_b are the bottom velocity in x and y directions, respectively; and $\mathbf{u}_{bh} = (u_b, v_b, 0)$.

The model is initialized with an along-shelf uniform density field (Fig. 3) consisting of isopycnals sloping up from the shelf break to the offshore surface, capturing main features of the wintertime MAB shelf break density distribution (Linder and Gawarkiewicz 1998; Zhang et al. 2011). The two-dimensional (2D) cross-shelf density structure is generated with

$$\eta_1 = \frac{1}{2} + \frac{1}{2}\tanh\left(\frac{y - y_0 + W_1}{W_0}\right), \qquad (21a)$$

$$\eta_2 = -2 + 2\tanh\left(\frac{y - y_0}{\eta_1 W_2}\right), \qquad (21b)$$

$$\eta_3 = \frac{1}{2} - \frac{1}{2}\tanh\left(\frac{z - z_0}{D} + \eta_2\right), \quad \text{and} \qquad (21c)$$

$$\rho = \rho_1 + [\rho_2 - \rho_1 + \rho_b(z)]\eta_3. \qquad (21d)$$

In this formulation, density varies from $\rho_d(z) = \rho_2 + \rho_b(z)$ in the deep sea to ρ_1 at the onshore boundary. Here, ρ_2 is the surface density in the deep sea, and $\rho_b(z)$ is a vertical profile of density anomaly representing the background stratification below 100 m ($\rho_b = 0$ in the surface 100 m). The density difference of surface waters on the shelf and in the deep sea is $\Delta\rho = \rho_2 - \rho_1$. The hyperbolic tangent function in (21a) sets up a background variation field of length scale W_0. It is used in (21b) to generate asymmetrical cross-shelf density gradients on the onshore and offshore sides of the front with W_2 being the variation length scale. Here, y_0 corresponds to the y coordinate of the central isopycnal $\rho_c = (\rho_1 + \rho_2)/2$ on the surface. The offset of the centers of the hyperbolic tangent functions in (21a) and (21b), W_1, controls the near-surface slope of the frontal isopycnals and determines the density gradient asymmetry. Equation (21c) generates the vertical density gradient with

the vertical scale D, and z_0 corresponds to the resting depth of the central isopycnal in the absence of shelf topography. This density formulation is built upon that of Morgan (1997) with the addition of (21b) to generate the asymmetrical cross-shelf density gradients and a surface mixed layer deeper in the slope sea than on the shelf, a persistent feature of the MAB shelf break (Zhang et al. 2013). A 5-m bottom boundary layer with vertically uniform density is also imposed.

In this study, $\rho_b(z)$ is a stable profile ($\partial\rho_b/\partial z < 0$) obtained from a regional climatological density profile (Zhang et al. 2011); $\rho_2 = 1026.7 \text{ kg s}^{-1}$, $W_0 = 20 \text{ km}$, and $D = 45 \text{ m}$ are kept fixed. This leaves four control parameters for the density distribution: ρ_1, y_0, W_1, and W_2 (Table 1). Note that varying ρ_1 alters frontal buoyancy frequency N, which in this study is defined as the area-averaged buoyancy frequency in the upper 40 m of the frontal region bounded horizontally by the isopycnals of $\rho_c \pm 0.45\Delta\rho$, that is, $N = [-g/(\rho_0 A)\iint_A (\partial\rho/\partial z)\, dy\, dz]^{1/2}$, with A being the area surrounded by $\rho = \rho_c \pm 0.45\Delta\rho$ and $z = 0$ and 40 m. The depth of 40 m is chosen to be consistent with the wintertime surface mixed layer depth in the immediate vicinity of the MAB shelfbreak front (Zhang et al. 2013). Varying y_0 slides the front onshore or offshore, which, because of the sloping bottom, changes both the vertical and cross-shelf extents of the central isopycnal, H, and L_T (Fig. 1). Varying W_1 changes the slope of the frontal isopycnals and then N and L_T. Varying W_2 changes the frontal width and thus L, half-width of the front (Fig. 1).

Control values of the parameters (Table 1) are chosen to produce a typical wintertime MAB shelfbreak front (Fig. 3a) with $f = 0.937 \times 10^{-4} \text{ s}^{-1}$, $N = 6 \times 10^{-3} \text{ s}^{-1}$, $L_T = 14 \text{ km}$, $H = 90 \text{ m}$, and $L = 5 \text{ km}$. The corresponding along-shelf velocity u_0 computed with thermal wind balance and zero bottom velocity has a maximum speed of $|u_0|_{\max} = 0.39 \text{ m s}^{-1}$. The meridional width of the surface shear zone on the offshore side of the jet $l_s(z = 0) \approx L = 5 \text{ km}$ is narrower than that on the onshore side, and the relative vorticity on the offshore side of the jet $-du_0/dy \approx 8 \times 10^{-5} \text{ s}^{-1}$. These flow speeds and shear are also typical values observed at the MAB shelfbreak front (Fratantoni et al. 2001; Gawarkiewicz et al. 2001).

To validate the formulated relationships of meander length scale and perturbation growth rate with the sensitivity parameters (f, N, H, L, and L_T; see section 4c), we perform sensitivity simulations initialized with different density and velocity distribution. For this, we choose a set of control parameters (f, ρ_1, y_0, W_1, and W_2) that determines values of the sensitivity parameters and also contains the same degrees of freedom as the sensitivity parameter set. Within each of the five series of
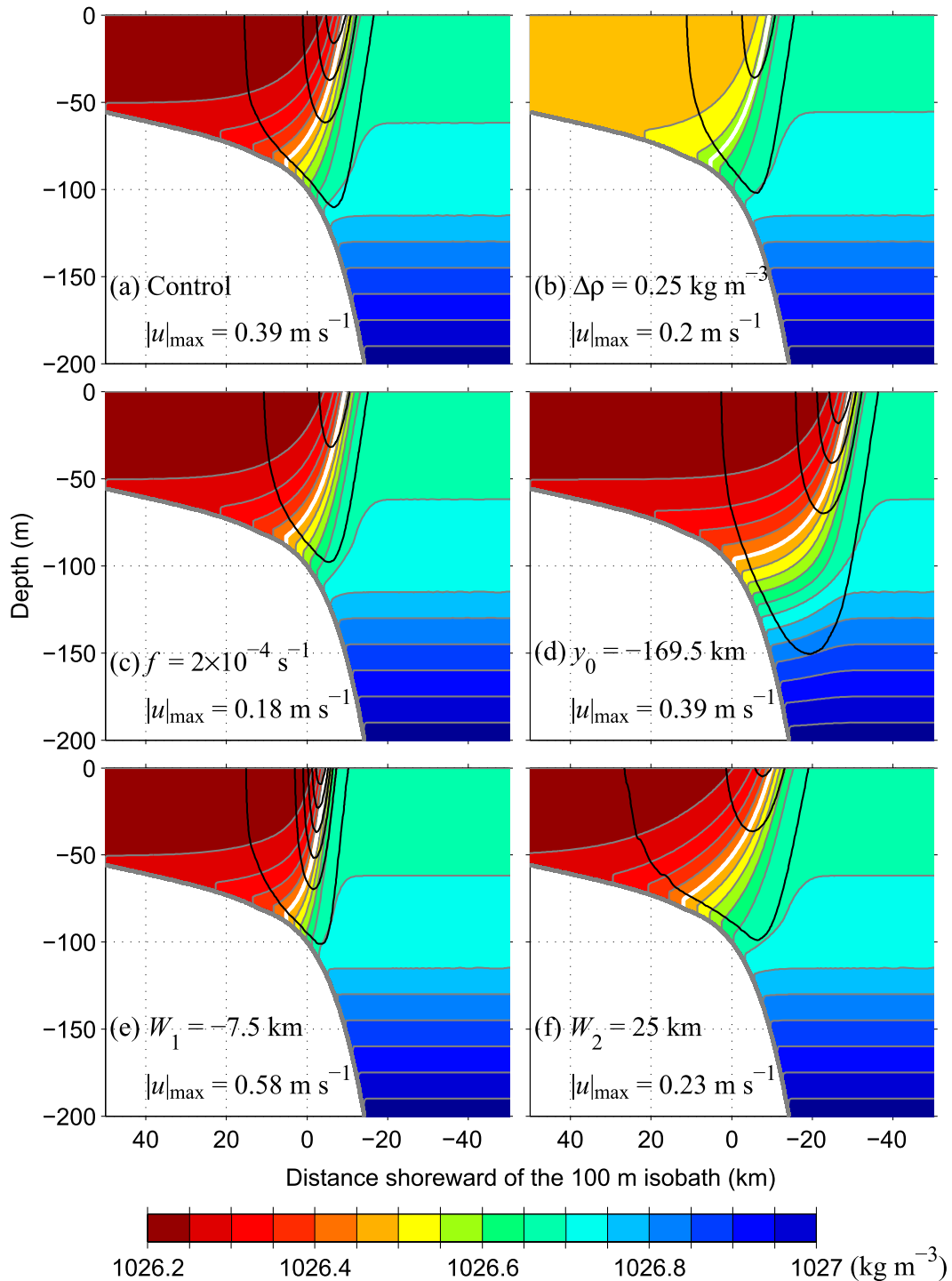
FIG. 3. Cross-shelf distribution of the initial density (color) and the thermal wind–balanced along-shelf velocity (black contour) in (a) the control case and (b)–(f) one case from each of five sensitivity series. The thick white line in each panel indicates the central isopycnal of $(\rho_1 + \rho_2)/2$. The velocity contours start from $-0.01\,\mathrm{m\,s^{-1}}$ and have an interval of $-0.1\,\mathrm{m\,s^{-1}}$. Values of the altered control parameter and the maximum along-shelf velocity $|u|_{\max}$ in each case are given.

TABLE 1. Model control parameters.

Symbol	Control parameter	Unit	Control value	Max value	Min value	Sensitivity parameter being influenced
f	Coriolis	$10^{-4}\,\mathrm{s}^{-1}$	0.937	2	0.5	f
ρ_1	Shelf surface density	$\mathrm{kg\,m}^{-3}$	1026.2	1026.575	1025.7	N
y_0	Cross-shelf location	km	-149.5	-129.5	-209.5	H and L_T
W_1	Frontal width 1	km	0	20	-10	L and L_T
W_2	Frontal width 2	km	15	25	10	L

density and velocity distributions (Fig. 3), only the value of the targeted control parameter is altered (see Table 1 for the variation range), and all other control parameters are kept the same as in the control simulation. There are a total of 33 different 2D density and velocity distributions, each of which is expanded along shelf to generate 3D model initial conditions.

The initial value of the vertical velocity $w_0 = 0$ everywhere in all simulations. The initial value of the cross-shelf velocity v_0 away from the front is zero, and that in the front is assigned with random values to facilitate the generation of frontal instability. The distribution of the random values is Gaussian with zero mean and standard deviation (STD) decreasing linearly from $\mathrm{STD}(v_0)$ at the core of the shelfbreak jet to 0 at the edges of the front. $\mathrm{STD}(v_0) = 0.002\,\mathrm{m\,s}^{-1}$ in all simulations, unless otherwise noted. This small value of $\mathrm{STD}(v_0)$ is chosen to ensure the linear development of the frontal instability in the initial stage.

Periodic conditions are applied on the east and west boundaries. The northern coastal boundary is a solid wall. The southern deep sea boundary is open with the Chapman (1985), Flather (1976), and Orlanski-type radiation (Orlanski 1976) conditions used for sea level, 2D momentum, and 3D variables, respectively. Horizontal viscosity and diffusivity are 0 in the study area and increase linearly in the sponge layer, reaching $100\,\mathrm{m}^2\,\mathrm{s}^{-1}$ at the southern boundary. The general length scale vertical turbulence closure k–kl scheme (Warner et al. 2005) and bottom drag coefficient $C_d = 0.003$ are used in all simulations, unless otherwise noted. There is no surface forcing. The model simulates the evolution of the shelfbreak fronts driven purely by internal dynamics. Each simulation runs for 120 days and by then the total available mean potential energy in the domain reaches a quasi-equilibrium state (see below).

4. Results

a. General pattern in the control simulation

The control case shelfbreak front has initial potential vorticity $\Pi > 0$ and $\Pi f > 0$ everywhere in the domain. The development of symmetric instability is hence not expected. Time series of the control case solution (Fig. 4) shows small-amplitude frontal instability with wavelengths of $\sim 30\,\mathrm{km}$ on day 24, which grows into finite-amplitude meanders on day 38 and forms eddies after that. As more eddies detach from the front and move in a disorganized fashion, the front loses its coherence.
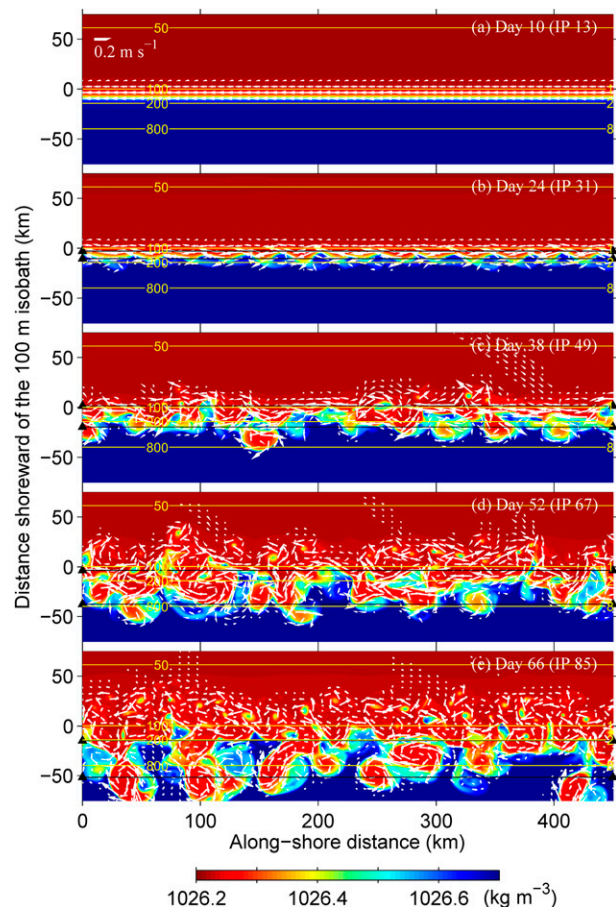

FIG. 4. Time series of density (color) and horizontal velocity (white arrows) at 10 m below the surface from the control simulation. Velocity arrows with speeds of less than $0.02\,\mathrm{m\,s}^{-1}$ are omitted, and the velocity scale is given at the upper-left corner of (a). The black lines and triangles indicate the frontal perturbation zones for computing the along-shelf length scale (see text); the yellow lines are the isobath contours. IP in the legend stands for inertial period.

During this process the length scale of the along-shelf variation, as reflected initially by the distances between troughs of the meanders and later by the distances between the eddy cores, becomes more variable, from hardly any variation around 30 km on day 24 to a range of 20–70 km on day 66. This simulated meander development takes a longer time than the $O(1)$ day growth window in the real ocean (Figs. 2a,b) for a number of reasons, including the lack of irregular topography and weak initial perturbation in the model (section 4d).

To examine the energetics of the frontal system, we compute the following volume-integrated energy quantities from the model output at each time:

Mean kinetic energy (MKE)

$$= \frac{\rho_0}{2} \int_{-L_{y0}}^{0} \int_{0}^{L_x} \int_{-h}^{0} (U^2 + V^2) \, dz \, dx \, dy, \tag{22a}$$

Available mean potential energy (AMPE)

$$= g \int_{-L_{y0}}^{0} \int_{0}^{L_x} \int_{-h}^{0} \int_{z-\zeta(z)}^{z} [\overline{\rho}(y, z) - \rho_d(z')] \, dz' \, dz \, dx \, dy, \tag{22b}$$

Eddy kinetic energy (EKE)

$$= \frac{\rho_0}{2} \int_{-L_{y0}}^{0} \int_{0}^{L_x} \int_{-h}^{0} (u'^2 + v'^2) \, dz \, dx \, dy, \tag{22c}$$

Available eddy potential energy (AEPE) $= g \int_{-L_{y0}}^{0} \int_{0}^{L_x} \int_{-h}^{0} \int_{z-\zeta'(z)}^{z} [\rho(x, y, z) - \overline{\rho}(y, z')] \, dz' \, dz \, dx \, dy,$ and $\quad$ (22d)

Eddy total energy (ETE) = EKE + AEPE. $\quad$ (22e)

Here, $U = L_x^{-1} \int_0^{L_x} u(x, y, z) \, dx$, $V = L_x^{-1} \int_0^{L_x} v(x, y, z) \, dx$, and $\overline{\rho}(y, z) = L_x^{-1} \int_0^{L_x} \rho(x, y, z) \, dx$; $u' = u(x, y, z) - U(y, z)$, $v' = v(x, y, z) - V(y, z)$; $\zeta(z)$ is vertical displacement of $\overline{\rho}(y, z)$ with respect to the far-field density $\rho_d(z)$; and $\zeta'(z)$ is vertical displacement of $\rho(x, y, z)$ with respect to $\overline{\rho}(y, z)$. Here, $\zeta(z)$ and $\zeta'(z)$ are defined positive upward and negative downward. Note that the available potential energy calculations in (22b) and (22d) are based on a coordinate-independent formula (Holliday and McIntyre 1981; Kang and Fringer 2010; Lamb 2008) to avoid the ambiguous choice of a reference depth. It is positive definite for a stable reference density profile (Holliday and McIntyre 1981), as in this case with $\partial \rho_d / \partial z < 0$ and $\partial \overline{\rho} / \partial z < 0$. Because the model domain is open at the offshore end, the far-field density $\rho_d(z)$ is used as the reference density profile in (22b) (Lamb 2008). Because only a small portion of the AMPE is released within the 120-day simulation, AMPE is always much greater than the other energy quantities, and the AMPE anomaly relative to AMPE on day 120 are presented here.

Mixing-induced energy dissipation over the time scale of interest ($\sim$50 days) is negligible as the total mechanical energy (MKE + AMPE + EKE + AEPE) in the model has almost no change in the first 50 days. Simulations with constant minimum vertical mixing ($\kappa = \kappa_\theta = 10^{-5}$ m^2 s^{-1}) also show no significant change in the meander pattern in the first 50 days from those using a turbulence closure. Thus, temporal variation of the energy quantities (Fig. 5a) reflects mostly energy transfer associated with the frontal evolution. During the initial development stage (before day 25), EKE, AEPE, and ETE all experienced a period of exponential growth. We compute the initial growth rate σ_m as the averaged rate of exponential growth over the period $[t_1, t_2]$:

$$\sigma_m = \frac{\ln[\text{ETE}(t_2)/\text{ETE}(t_1)]}{t_2 - t_1}. \tag{23}$$

Here, $t_1 = 1$ day and $t_2 = 25$ days. In the control simulation, $\sigma_m \approx 0.31$ day$^{-1} \approx 0.04f$.

Starting at about day 20 when the frontal meanders become visible, the total MKE and AMPE decrease, while EKE and AEPE increase (Fig. 5). They all reach quasi-equilibrium states by the end of the simulation. The same temporal patterns are shown in cross-shelf distributions of the along-shelf and vertically integrated MKE and EKE density (Fig. 6), $\text{MKE}_y(y, t)$, and $\text{EKE}_y(y, t)$, respectively. After day 20, the region of nonzero EKE_y expands in the cross-shelf direction (Fig. 6b). The simultaneous decrease of MKE and AMPE after day 20 suggests that both barotropic and baroclinic instability occur as the perturbation grows. Meanwhile, the EKE increase in the first 50 days is $\sim$4 times that of the MKE reduction over the same period, indicating the dominance of baroclinic instability.

To obtain a representative along-shelf length scale of the modeled finite-amplitude frontal meanders, we take the following quantitative steps that are designed for fair comparisons of the length scales from different simulations (section 4c):
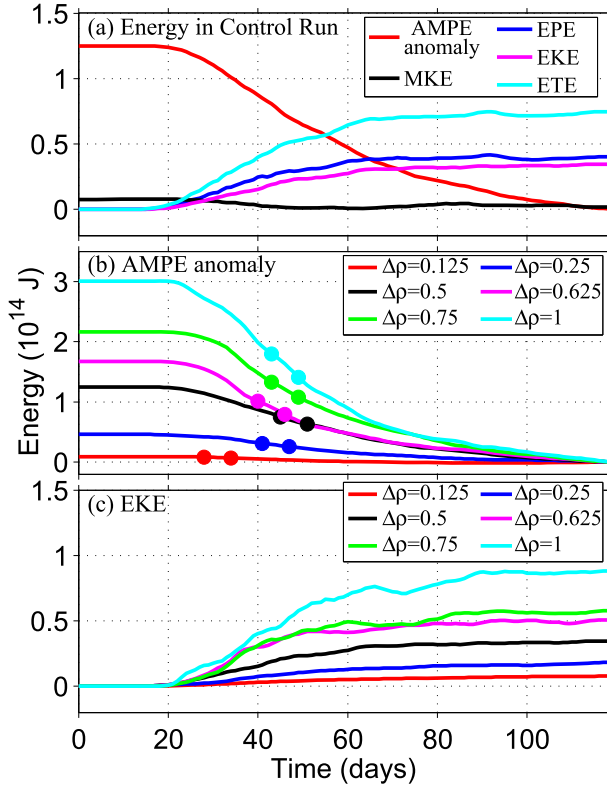
FIG. 5. Time series of the volume-integrated (a) AMPE anomaly, MKE, AEPE, EKE, and ETE in the control simulation; (b) AMPE anomaly and (c) EKE in the simulations of different $\Delta\rho$ (kg m^{-3}). The circles in (b) indicate the examination windows of five inertial periods for calculating length scales of along-shelf variability.

1) We first identify the frontal perturbation zone as the cross-shelf region with EKE$_y$ values greater than 60% of the cross-shelf peak value at each time (Fig. 6). The frontal perturbation zone broadens with frontal instability growth and gradually migrates offshore after day 40. Much of the offshore migration at the later stage is caused by offshore motions of eddies.

2) We then compute the along-shelf structure function

$$Q(\Delta x, t) = \langle\langle[\rho_{10}(x + \Delta x, y, t) - \rho_{10}(x, y, t)]^2\rangle_x\rangle_y, \quad (24)$$

as the mean-square difference of ρ_{10} (density at 10 m below surface) separated by an along-shelf distance Δx (e.g., Todd et al. 2013). Here, $\langle\cdot\rangle_x$ denotes averaging in x over $[0, L_x - \Delta x]$ for each Δx, and $\langle\cdot\rangle_y$ denotes averaging in y over the identified frontal perturbation zone. The structure function within days [20, 35] oscillates with Δx (Fig. 7a), reflecting the periodic frontal instability at the initial stage (Fig. 4b). Starting from day 35, the oscillation length scale increases gradually as the frontal perturbation grows and meanders widen (Fig. 4c). After day 65,
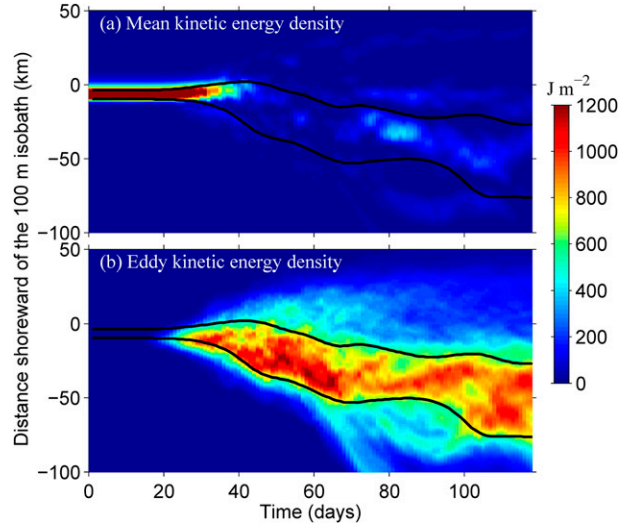

FIG. 6. Time series of the cross-shelf distribution of along-shelf and vertically integrated (a) MKE and (b) EKE density (MKE$_y$ and EKE$_y$, respectively) in the control simulation. The black lines outline the region of >60% of the cross-shelf maximum EKE$_y$ at each time, which is defined as the frontal perturbation zone.

the oscillation length scale varies dramatically in time as eddies detach from the front and dominate the along-shelf variability (Fig. 4e).

3) In the third step, we identify the first trough of the structure function (corresponding to the first secondary maximum of an autocorrelation curve) at each time after the AMPE reduction reaches 2% of the maximum reduction. Time evolution of the corresponding length scale forms a time series $r_1(t)$. We
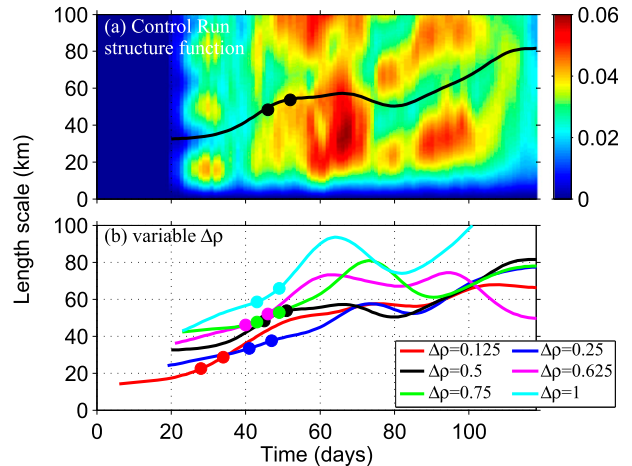

FIG. 7. (a) Time series of the structure function (color) and along-shelf length scale (black line) in the control simulation; (b) time series of the along-shelf length scale in the simulations of different $\Delta\rho$ (kg m^{-3}). Circles indicate the examination windows of five inertial periods for computing the length scale of along-shelf variability in each case.

then apply a one-dimensional low-pass Gaussian filter with a cutoff frequency of $(14 \text{ day})^{-1}$ to $r_1(t)$ to remove the high-frequency variations that are associated with individual eddy events. The smoothed time series $R_1(t)$ generally captures the low-frequency variation of the frontal length scale (Fig. 7a).

4) In this last step, we average $R_1(t)$ over a window of five inertial periods (hereinafter referred to as the examination window) that starts at the time T_e when AMPE reduction reaches e^{-1} of the maximum reduction in the simulation period (Fig. 7a). The averaged $R_1(t)$ value is used as modeled meander length scale λ_m. The factor e^{-1} is chosen to place the examination window at the meander stage that is after the initial small-amplitude development and before the complete domination of disorganized eddies.

Application of these steps to the control simulation gives $\lambda_m = 51$ km, close to the 33–50-km range of length scale observed at the MAB shelf break (Garvine et al. 1988; Gawarkiewicz et al. 2004; Todd et al. 2013).

b. Analytical scalings

1) MEANDER LENGTH SCALE

To derive a formula for the along-shelf meander length scale that is directly applicable to observational studies, we take a pragmatic approach by combining theoretical length scales of linear barotropic and baroclinic instability within the context of a shelfbreak front. One assumption here is the proportionality between the frontal meander length scale and the wavelength of the initial frontal linear instability. As frontal meanders develop from the linear instability, the linear instability wavelength strongly influences the meander length scale (see section 4c). But because meander flows are nonlinear and eventually deform into eddies, other length scales (e.g., baroclinic Rossby radius of deformation) may also influence its length scale. The relative importance of these different influences on the meander length scale is unclear. However, as the baroclinic Rossby radius of deformation has the same scale as the dominant wavelength of the linear baroclinic instability (section 2a), its influence is implicitly embedded in the below formulation of the meander length scale.

We first examine the relevancy of barotropic and baroclinic instability at the shelfbreak front by comparing their control case length scales and growth rates qualitatively estimated using the formulas in section 2. Because horizontal shear on the offshore side of the jet is stronger than that on the onshore side, barotropic instability presumably develops faster on the offshore side. As the width of the shear zone $l_s(z)$ shrinks with

depth and reaches 0 on the bottom, we consider its vertical mean as the effective shear width for the development of barotropic instability, that is, $L_s \approx l_s(z = 0)/2$. From (11), we obtain the along-shelf wavelength of the fastest-growing barotropic perturbation:

$$\lambda_{bt} = \frac{2\pi}{k_{bt}} \approx \frac{\pi l_s(0)}{0.7968}. \qquad (25)$$

Substituting $l_s(0) = 5$ km into (25) gives the control-case, along-shelf length scale of the frontal barotropic instability $\lambda_{bt0} \approx 20$ km. Substituting $|dU/dy| = -du_0/dy \approx 8 \times 10^{-5} \text{s}^{-1}$ into (10) gives the growth rate of the barotropic instability $\sigma_{bt0} \approx 1.6 \times 10^{-5} \text{s}^{-1}$. For baroclinic instability, as $m_{bc} = \pi/L$, $m_{bc}NH/(2f) \approx 0.65$ in the control case, and the maximum perturbation growth is achieved at $NHk_{bc}/(2f) \approx 0.6$ (Fig. 13.3 in Gill 1982). The length scale of the baroclinic instability is then $\lambda_{bc0} = 2\pi/k_{bc} \approx 30$ km. Equation (7) gives the corresponding growth rate $\sigma_{bc0} \approx 2.0 \times 10^{-5} \text{s}^{-1}$. Thus, σ_{bt0} and σ_{bc0} are of the same order of magnitude and $\lambda_{bc0} > \lambda_{bt0}$.

For a retrograde shelfbreak front, Lozier and Reed (2005) argued that both barotropic and baroclinic instability play a role in the frontal instability. This claim is supported here by the modeled simultaneous reduction of AMPE and MKE (Fig. 5a) and the estimated σ_{bt0} and σ_{bc0} being close. Meanwhile, the modeled EKE increase in the first 50 days being ~3 times larger than the MKE decrease indicates the dominance of baroclinic instability (Fig. 5a) and thus $C_{bt}/C_{bc} = S < 1$. For the shelfbreak front of interest (Fig. 1), the horizontal length scale for estimating C_{bt}/C_{bc} should contain both L and L_T, rather than only L or only L_T, that is,

$$S = \frac{C_{bt}}{C_{bc}} = \left[\frac{NH}{f(L + L_T)} \right]^2. \qquad (26)$$

This is reflected in the following relationships: (i) with fixed L and increasing L_T, frontal isopycnals move away from the shelf into the deep ocean with a water depth much greater than the frontal depth H and frontal instability becomes more baroclinic with decreasing C_{bt}/C_{bc}; (ii) at the limit of $L \rightarrow 0$, a shelfbreak front of finite L_T remains baroclinic with finite C_{bt}/C_{bc}; and (iii) at the limit of $L_T \rightarrow 0$, a shelfbreak front of finite L remains baroclinic with finite C_{bt}/C_{bc}.

From (9) and (11) we have the length scales of the baroclinic instability

$$\lambda_{bc} \propto NH/f, \qquad (27)$$

and that of the barotropic instability

$$\lambda_{\mathrm{bt}} \propto L_s \approx L. \qquad (28)$$

Hence,

$$\frac{\lambda_{\mathrm{bt}}}{\lambda_{\mathrm{bc}}} \propto \frac{fL}{NH}. \qquad (29)$$

Because of the dominant role of baroclinic instability, the along-shelf length scale of the mixed frontal instability can be formulated as

$$\lambda_s = c_{\mathrm{bt}}\lambda_{\mathrm{bc}} \propto c_{\mathrm{bt}}NH/f. \qquad (30)$$

Here, the nondimensional coefficient c_{bt} represents the influence of barotropic instability, and it (i) decreases with increasing influence of barotropic instability, that is, increasing $C_{\mathrm{bt}}/C_{\mathrm{bc}}$ and S, since $\lambda_{\mathrm{bt}} < \lambda_{\mathrm{bc}}$ and (ii) satisfies (27) and (28) at the limits of pure baroclinic and barotropic instability, respectively. Given these, an appropriate expression of c_{bt} is

$$c_{\mathrm{bt}} = \frac{1}{1 + a_1 S^{1/2}}. \qquad (31)$$

Substituting (31) into (30) gives

$$\lambda_s = \frac{b_1}{1 + a_1 S^{1/2}} \frac{NH}{f}. \qquad (32)$$

Here, a_1 and b_1 are empirical constants. Toward the limit of pure barotropic instability, $L + L_T \to 0$, $S \to \infty$, $c_{\mathrm{bt}} \propto S^{-1/2}$, and thus $\lambda_s \propto L + L_T \approx L$; toward the limit of pure baroclinic instability, $L + L_T \to \infty$, $S \to 0$, and thus $\lambda_s \propto NH/f$.

2) GROWTH RATE

We seek to derive a formula for the growth rate of the mixed frontal instability during the initial stage of exponential growth. In addition to the growth rates of linear barotropic and baroclinic instability, we consider the stabilizing effect of bottom slope (Blumsack and Gierasch 1972; Brink 2012). Symmetric instability is not included here because it generally grows faster (Boccaletti et al. 2007; Brink and Cherian 2013) and develops separately from barotropic or baroclinic instability. We will discuss frontal symmetric instability separately in section 4c.

From the thermal wind balance, we have $\partial u/\partial z = -(g/f)(\partial \rho/\partial y) = -(g/f)(\partial \rho/\partial z)|_y (\partial z/\partial y)|_{\rho_c}$, which gives a scale of along-shelf velocity:

$$U \propto N^2 H^2/(fL). \qquad (33)$$

Substituting it into (7), we obtain a scale of the growth rate of baroclinic instability:

$$\sigma_{\mathrm{bc}} \propto NH/L. \qquad (34)$$

Note that the corresponding nondimensional growth rate σ_{bc}/f is proportional to $S^{1/2}$ of the baroclinic flow considered by Gill (1982).

Assuming zero bottom velocity, the horizontal shear of the thermal wind–balanced along-shelf velocity causes the barotropic instability. Substituting (33) into (10) gives a scale of the growth rate of barotropic instability:

$$\sigma_{\mathrm{bt}} \propto N^2 H^2/(fL^2). \qquad (35)$$

Following these, we express a scale of the growth rate of the shelfbreak frontal instability as

$$\sigma_s \propto \sigma_{s0}q = c_{\mathrm{bt}}^{-1}\sigma_{\mathrm{bc}}q. \qquad (36)$$

Here, $\sigma_{s0} = c_{\mathrm{bt}}^{-1}\sigma_{\mathrm{bc}}$ is a scale of the instability growth rate of a front on a flat bottom, and q is a nondimensional coefficient representing the stabilizing effect of a sloping bottom.

We assume the same imaginary perturbation wave speed in barotropic and baroclinic instability, and the influences of barotropic instability on the wavelength and growth rate of the frontal instability are then inverse to each other. The c_{bt} factor in (30) is thus translated into (36) as $c_{\mathrm{bt}}^{-1} = (1 + a_1 S^{1/2})$. This choice of the factor also makes σ_{s0} satisfy (34) and (35) at the limits of pure barotropic and baroclinic instability, respectively: as $L + L_T \to 0$ and $L + L_T \approx L$, $S \to \infty$, $c_{\mathrm{bt}}^{-1} \propto S^{1/2}$, and thus $\sigma_{s0} \propto N^2 H^2/(fL^2)$, and as $L + L_T \to \infty$ and $S \to 0$, $\sigma_{s0} \propto NH/L$.

The influence of a bottom of constant gentle slope α and infinite cross-stream extent on baroclinic instability is often incorporated into scalings in the form of a slope Burger number (e.g., Brink 2012; Brink and Cherian 2013):

$$s = \alpha N/f. \qquad (37)$$

The gentle shelf slope in this study extends only to the shelf break, beyond which the seafloor drops rapidly to a much greater depth. As L_T increases and the sloping isopycnals move offshore away from the shelf break, the effect of the shelfbreak sloping bottom on the frontal instability presumably diminishes. Hereby, we incorporate the frontal aspect ratio $H/(L + L_T)$ into the bottom effect formulation to take into account both the stabilizing effect of bottom slope and the horizontal distance between the front and shelf break, that is,

$$q = \frac{1}{1 + a_2 sH/(L + L_T)} = \frac{1}{1 + a_2 \alpha S^{1/2}}. \qquad (38)$$

Here, a_2 is an empirical constant. Note that (38) satisfies the limit of no bottom effect ($q \to 1$) at $L + L_T \to \infty$.
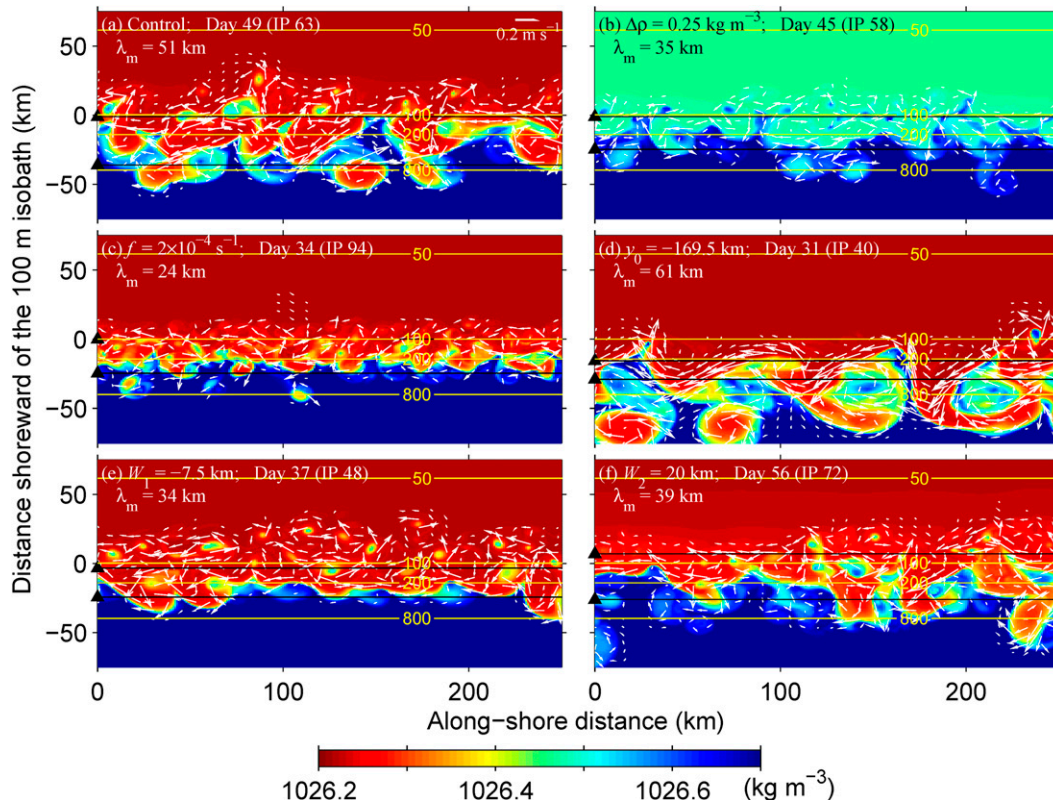
FIG. 8. The 10-m density (color) and horizontal velocity (white arrows) at the center of the examination window of the (a) control simulation and (b)–(f) one simulation from each of the sensitivity series. Velocity arrows with speeds of less than $0.02\,\mathrm{m\,s^{-1}}$ are omitted, and the velocity scale is given at the upper-right corner of (a). The black lines and triangles indicate the frontal perturbation zones for computing the along-shelf length scales; the yellow lines are the isobath contours. Values of the altered control parameter and computed length scale in each case are given. Note that only part of the model domain is shown here.

Substituting (31), (34), and (38) into (36) gives a formula of the growth rate of the shelfbreak frontal instability:

$$\sigma_s = b_2 \frac{1 + a_1 S^{1/2}}{1 + a_2 \alpha S^{1/2}} \frac{NH}{L}, \qquad (39)$$

with b_2 being another empirical constant.

In the next subsection, we will compare the formulas in (32) and (39) with results of the sensitivity simulations and determine the values of a_1, b_1, a_2, and b_2 empirically.

c. Sensitivity simulations for verification of the scalings

For each of the sensitivity simulations, we compute the perturbation growth rate σ_m and the meander length scale λ_m, following the procedures described in section 4a. Variations of σ_m and λ_m among the simulations reflect the influence of the sensitivity parameters. Here, we use the simulations of different $\Delta\rho$ (i.e., ρ_1) to show dependence of σ_m and λ_m on the parameters (Figs. 5, 7, 8, 9).

The evolution of the AMPE anomaly and EKE show clear dependence on $\Delta\rho$ (Figs. 5b,c). Increasing $\Delta\rho$ increases N and initial AMPE, which results in faster AMPE reduction and higher EKE in the end. As N increases from 2.9×10^{-3} to $8.5 \times 10^{-3}\,\mathrm{s^{-1}}$, σ_m increases from 0.25 to 0.34 day^{-1} (Fig. 9g) (still less than the inertial frequency, $f/2\pi \approx 1.3$ day^{-1}). Values of T_e vary little among the simulations, except for $\Delta\rho = 0.125\,\mathrm{kg\,m^{-3}}$ ($\rho_1 = 1026.575\,\mathrm{kg\,m^{-3}}$) having $T_e \sim 10$ days smaller than the rest (Fig. 5b). Figure 7b shows higher initial values of $R_1(t)$ for larger $\Delta\rho$, indicating a positive relationship between the initial perturbation length scale and N. The subsequent evolutions of $R_1(t)$ of all the simulations show similar trends of increases in the meander stage. This indicates a strong influence of initial linear instability wavelength on the meander length scale and supports the assumption in section 4b on proportionality between the linear instability wavelength and λ_m. Correspondingly, λ_m increases with increasing N (Fig. 9b). After day 65, evolutions of $R_1(t)$ become less coherent as the front breaks down into eddies with disorganized motions.
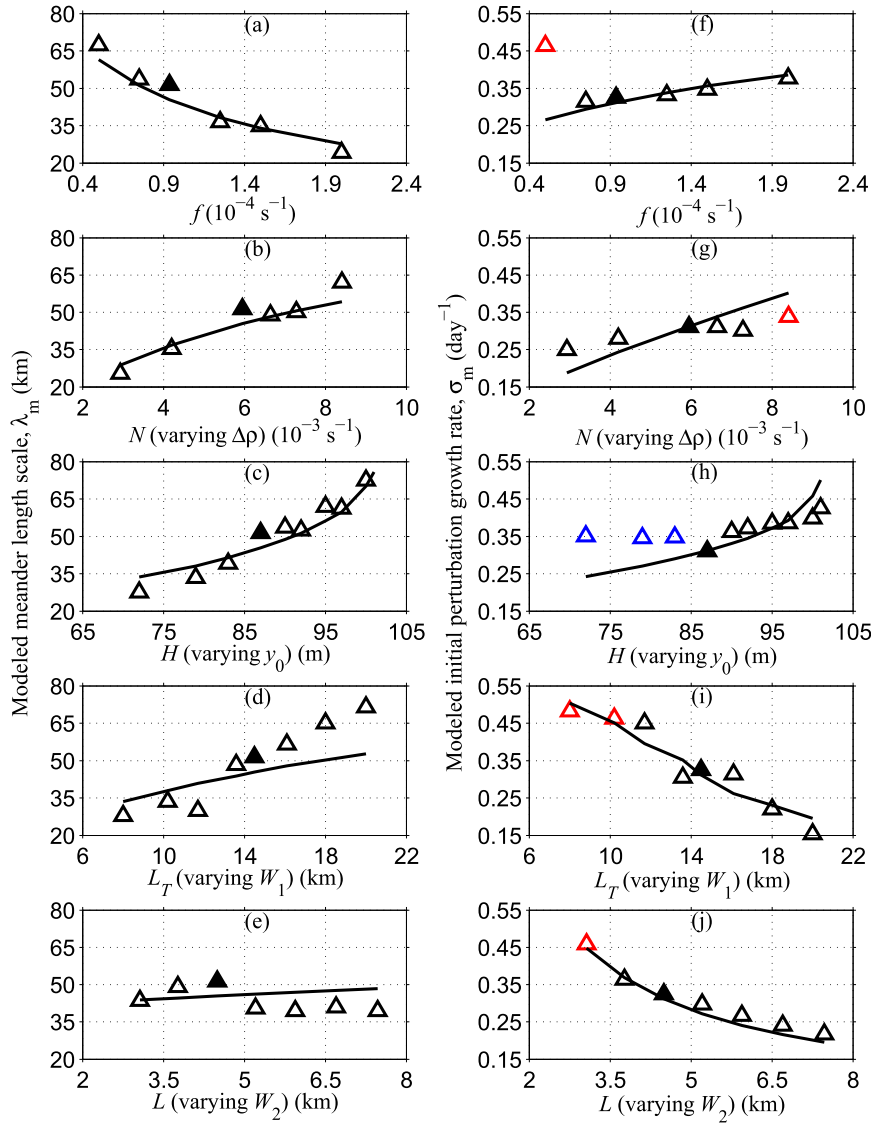
FIG. 9. Variation of modeled (a)–(e) along-shelf length scale and (f)–(j) initial perturbation growth rate with respect to different sensitivity parameters. The solid symbol in each panel represents the control simulation; the red and blue triangles in (f)–(j) represent the cases of initial development of symmetric instability in the surface and bottom boundary layers, respectively. The black lines represent the relationships of the length scale and growth rate with each parameter as described by (32) and (39), respectively.

We then examine the dependence of λ_m and σ_m on each of the sensitivity parameters (Figs. 8, 9). The pattern of λ_m versus the sensitivity parameters (Figs. 9a–e) is generally consistent with the relationships in (32): λ_m decreases with increasing f and increases with increasing N, H, and L_T, while the dependence of λ_m on L is ambiguously weak (Fig. 9e). Figures 10a and 10b show respectively the nondimensional and dimensional comparison of all λ_m with corresponding λ_s computed using values of the sensitivity parameters in (32). The nondimensional comparison, as normalized by $\lambda_{bc} \propto NH/f$,

depicts the deviation of the frontal instability from the baroclinic instability and validates the formulated influence of barotropic instability in (31). Both the nondimensional and dimensional comparisons collapse around a straight line with a general alignment of the results of different sensitivity series, except the one with altered frontal width W_2. Misalignment of the W_2 series occurs over a very small length scale range, slightly wider than the ± 1 root-mean-square error range. Given the weak dependence of λ_m on L (Fig. 9e), it is possible that this misalignment reflects merely uncertainty in the
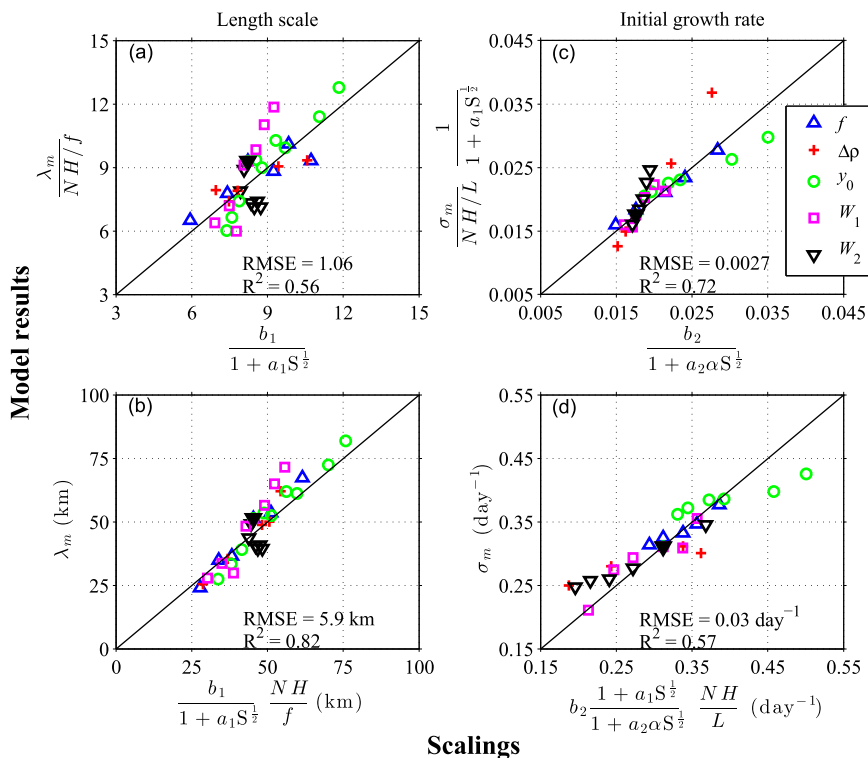
FIG. 10. Comparison of the modeled (left) along-shelf length scale and (right) initial per-turbation growth rate with values computed from the scaled relationships of (32) and (39), respectively, in both (top) nondimensional and (bottom) dimensional spaces. Each type of symbol represents comparisons obtained through varying one control parameter; the solid symbols represent the control simulation. A least squares fit of the nondimensional length scale gives $a_1 = 2.69$ and $b_1 = 14.65$, and that of the nondimensional growth rate gives $a_2 = 5.1 \times 10^3$ and $b_2 = 6.2 \times 10^{-2}$. The R^2 and root-mean-square error (RMSE) of the matches are given. All sensitivity simulations are included in (a) and (b), and the simulations with initial development of symmetric instability are excluded in (c) and (d).

estimated λ_m (section 4d). Least squares fitting (LSF) to the nondimensional comparison gives $a_1 = 2.69$ and $b_1 = 14.65$, and applying these value in (32) places the collapsed alignment around the diagonal line ($y = x$) in both non-dimensional and dimensional spaces (Figs. 10a,b). We emphasize that the alignments are not consequences of the LSF, as the nondimensional comparison collapses around a straight (off diagonal) line for any other values of a_1 and b_1. Rather, the alignments indicate consistency between the length scale formula and model frontal dy-namics in the parameter space that we have tested and demonstrate the validity of the formulated influence of barotropic instability on the frontal instability. Some scattering around the diagonal is present in both compar-isons, presumably caused by dynamics either neglected or oversimplified in the formulation (e.g., nonlinearity) or by uncertainty in the estimated λ_m.

The patterns of σ_m versus the sensitivity parameters (Figs. 9e–h) are more complex. Most of the results are consistent with the relationships in (38), including

negative dependence of σ_m on L and L_T. However, σ_m in a few of the f and y_0 series (Figs. 9f,h) are much larger than the scaled values and fall out of the formulated trends. For instance, when $f = 0.5 \times 10^{-4}\,\mathrm{s}^{-1}$, $\sigma_m = 0.47\,\mathrm{day}^{-1}$, much larger than σ_m from the other simu-lations in the f series but still less than the inertial fre-quency $f/2\pi = 0.69\,\mathrm{day}^{-1}$. Close examination of the simulation of $f = 0.5 \times 10^{-4}\,\mathrm{s}^{-1}$ reveals that its initial potential vorticity $\Pi_0 < 0$ in the surface 50 m of the frontal region (Fig. 11c), suggesting development of frontal symmetric instability. Consistently, the frontal instability in the first 2 days consists of frontal re-circulation cells that are nearly uniform in the along-shelf direction (Fig. 11d). In this case, $N = 6 \times 10^{-3}\,\mathrm{s}^{-1}$, $H = 90\,\mathrm{m}$, and $U = |u_0|_{\max} = 0.73\,\mathrm{m\,s}^{-1}$. Substituting these into (14) gives Ri = 0.55, favorable for the de-velopment of symmetric instability, and into (15) gives $\sigma_{\mathrm{si}} = 0.62\,\mathrm{day}^{-1}$, not too far from $\sigma_m = 0.47\,\mathrm{day}^{-1}$.

Because the initial flow of the symmetric instability is nearly along-shelf uniform, it does not directly
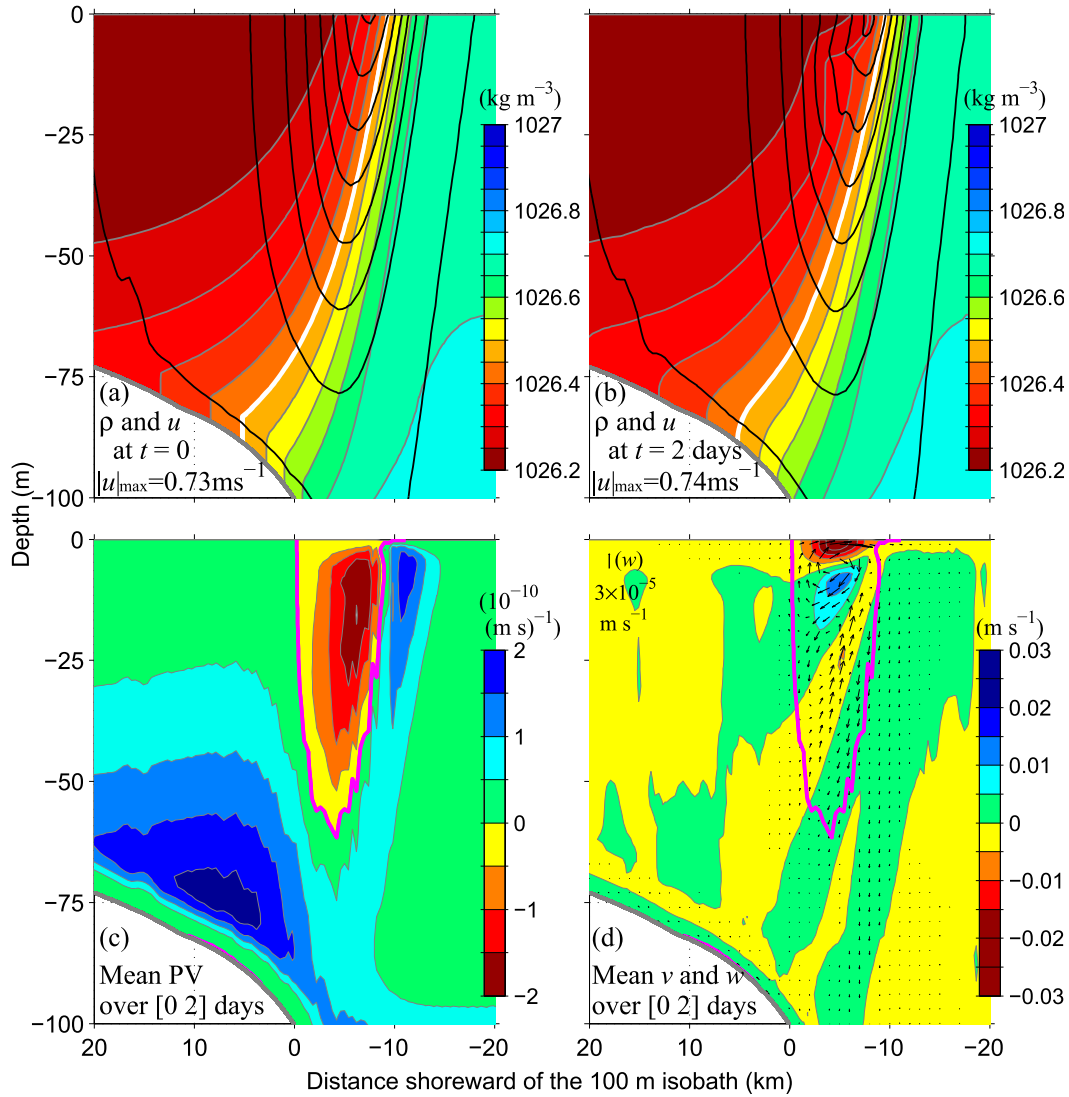
FIG. 11. Results from the sensitivity simulation of $f = 0.5 \times 10^{-4}\,\mathrm{s}^{-1}$: (top) cross-shelf sections of the density (color) and along-shelf velocity (black contour) at $t =$ (a) 0 and (b) 2 days; cross-shelf sections of the mean (c) potential vorticity and (d) secondary circulation over the first 2 days. In (a) and (b), the thick white lines depict the central isopycnal $(\rho_1 + \rho_2)/2$; the velocity contours start from $-0.01\,\mathrm{m\,s}^{-1}$ and have an interval of $-0.1\,\mathrm{m\,s}^{-1}$. (bottom) The magenta lines outline the region of negative potential vorticity. The color contour in (d) depicts the cross-shelf velocity, and the arrows depict both cross-shelf and vertical velocity. A scale of the vertical velocity is given at the upper-left corner of (d).

contribute to perturbation energy growth. However, a breakdown of the along-shelf uniformity by, for instance, initial baroclinic instability converts the strengthened cross-shelf flow to 3D perturbations and facilitates the subsequent development of baroclinic and barotropic instability. Meanwhile, λ_m of the simulation of $f = 0.5 \times 10^{-4}\,\mathrm{s}^{-1}$ follows the scaled trend of λ_s as well as the other simulations of varying f (Fig. 9a). It suggests that localized symmetric instability in the early stage does not affect the length scale of the frontal meanders

at the later stage, consistent with the finding of Brink and Cherian (2013).

We computed Π_0 for other simulations and found that all the simulations with σ_m deviating from the scaled trends (Figs. 9f–j) have the minimum potential vorticity $\Pi_{0\mathrm{min}} < 0$ in either the upper part of the front or the bottom boundary layer and that most of the other simulations have $\Pi_{0\mathrm{min}} > 0$ (Fig. 12). The values of σ_m of the simulations with $\Pi_{0\mathrm{min}} < 0$ are generally higher than the corresponding scaled values, except in the case of
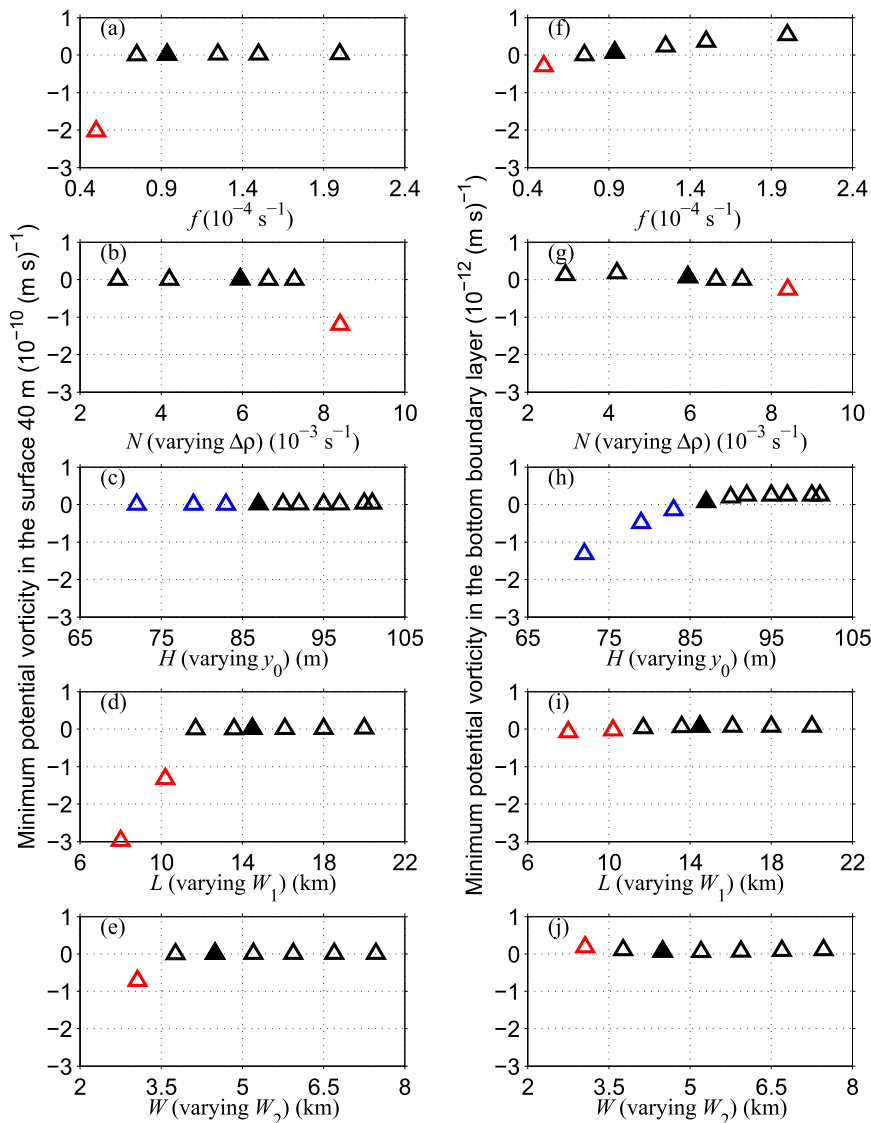
FIG. 12. Variation of the minimum initial potential vorticity in (left) the surface 40 m and (right) the bottom boundary layer with respect to different sensitivity parameters. The solid symbol in each panel represents the control simulation; the red and blue symbols represent the cases of negative minimum potential vorticity in the surface 40 m and in the bottom boundary layer, respectively.

$\Delta\rho = 1\,\mathrm{kg}\,\mathrm{m}^{-3}$ (Fig. 9g). Therefore, development of frontal symmetric instability is associated with the excessively high perturbation growth rates in some of the simulations.

As only barotropic and baroclinic instability are considered in the formulation of σ_s in (39), we exclude the simulations of $\Pi_{0\mathrm{min}} < 0$ from the comparison between σ_m and σ_s (Figs. 10c,d). The nondimensional comparison, as normalized by $\sigma_{s0} = c_{\mathrm{bt}}^{-1}\sigma_{\mathrm{bc}}$, depicts the deviation from the flat-bottom barotropic and baroclinic mixed frontal instability and therefore provide a validation for

the formulated influence of the shelfbreak sloping bottom in (38). Both nondimensional and dimensional comparisons collapse conveniently around a straight line. LSF to the nondimensional comparison gives $a_2 = 5.1 \times 10^3$ and $b_2 = 6.2 \times 10^{-2}$, and applying these values in (39) places the collapsed alignment around the diagonal for both nondimensional and dimensional comparisons. Note that the relatively large value of a_2 is consistent with incorporation of the frontal aspect ratio $H/(L + L_T) \sim O(10^{-3}\text{–}10^{-2})$ in (38). The match between the modeled and formulated growth rate indicates
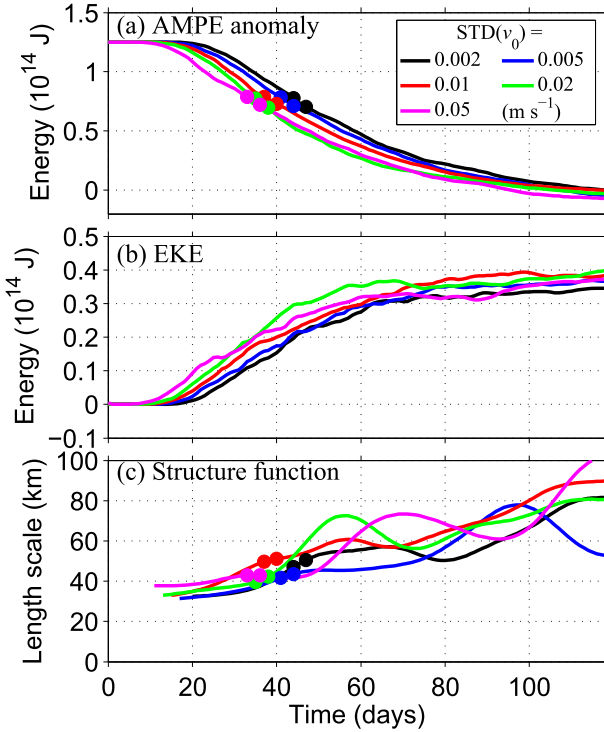
FIG. 13. Time series of the (a) total AMPE anomaly, (b) total EKE, and (c) $R_1(t)$ from simulations of different initial perturbation magnitude. The circles in (a) and (c) indicate the examination windows of five inertial periods. The black lines are obtained from the control simulation.

FIG. 14. As in Fig. 13, but from simulations of different quadratic bottom drag coefficients.

that (39) captures the main dynamics of the simulated perturbation growth, particularly the influence of bottom slope on frontal perturbation growth. Similar to the length scale comparison, scattering remains in both nondimensional and dimensional comparisons, likely indicating missing dynamics in the formulation.

d. Other sensitivity simulations

We conduct additional sensitivity simulations with respect to the initial perturbation strength $STD(v_0)$, bottom friction C_d, and bottom topography to examine how these factors affect the development of the frontal meanders. The results also shed light on the uncertainty in the modeled meander length scale λ_m. Note that analyzing the mechanisms of these factors influencing frontal instability is out of the scope of this work.

With increasing $STD(v_0)$, the meanders develop faster, as indicated by smaller T_e (Fig. 13a) and faster rate of EKE increasing (Fig. 13b). This provides an explanation for the simulated meander development being slower than in the real ocean (e.g., Figs. 2a,b). Perturbations in the real ocean, as induced by irregular topography, tides, surface forcing, or remote forcings, are often on the order of $0.1\,\mathrm{m\,s^{-1}}$, much stronger than the
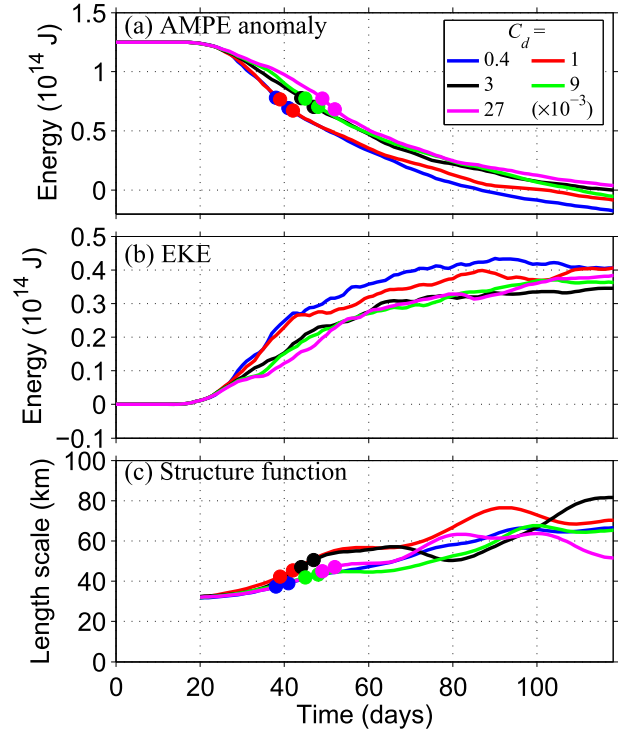
initial perturbation used in the model. Perturbations in the real ocean are often spatially coherent, which may also cause faster instability growth than the random perturbation used here. The term λ_m in these simulations varies within a range of $\pm 5\,\mathrm{km}$ from that in the control simulation with no clear trend (Fig. 13c) and is thus a likely reflection of the uncertainty in the λ_m estimate. Note that an error bar of $\pm 5\,\mathrm{km}$ for λ_m would cover most of the differences between λ_m and λ_s in Figs. 9a–e and explain much of the scattering in Figs. 10a and 10b.

With altered C_d, the EKE growth before day 20 stays the same, but T_e increases with increasing C_d (Fig. 14). This indicates that bottom friction does not influence the initial development of the frontal instability, but it affects the development of the finite-amplitude frontal meanders at a later stage. The modeled length scale λ_m varies with C_d within a range of $\pm 5\,\mathrm{km}$ without a clear trend, also a likely reflection of the uncertainty in the estimated λ_m.

For bottom topography, we consider the influence of shelfbreak canyons, an abundant and first-order topographic feature at many of the shelf edges, including the MAB shelf break (Allen and Durrieu de Madron 2009). The canyon topography is obtained by replacing y_h in (16) with

$$y_p = y_{p0} + \sum_{i}^{n_c} l_c \exp\left[-\frac{(x - x_{ci})^2}{2w_c^2}\right]. \qquad (40)$$

TABLE 2. Parameters for the shelfbreak canyon(s).

Simulation index	Number of canyons (n_c)	Canyon x position (x_c; km)	Length scale (l_c; km)	Width scale (w_c; km)
Canyon 1	1	240.25	10	5
Canyon 2	1	240.25	15	10
Canyon 3	2	215.25; 265.25	10	5

Here, $y_{p0} = -170.5$ km; n_c is the number of canyons; i is the canyon index; x_{ci} is the x coordinate of the canyon axis; and l_c and w_c are the canyon length and width scales, respectively. We conduct three simulations with different combinations of n_c, l_c, and w_c (Table 2), and the values of l_c and w_c are representative for the MAB shelfbreak canyons.

The inclusion of a shelfbreak canyon accelerates the development of frontal instability (Fig. 15 vs Fig. 4),
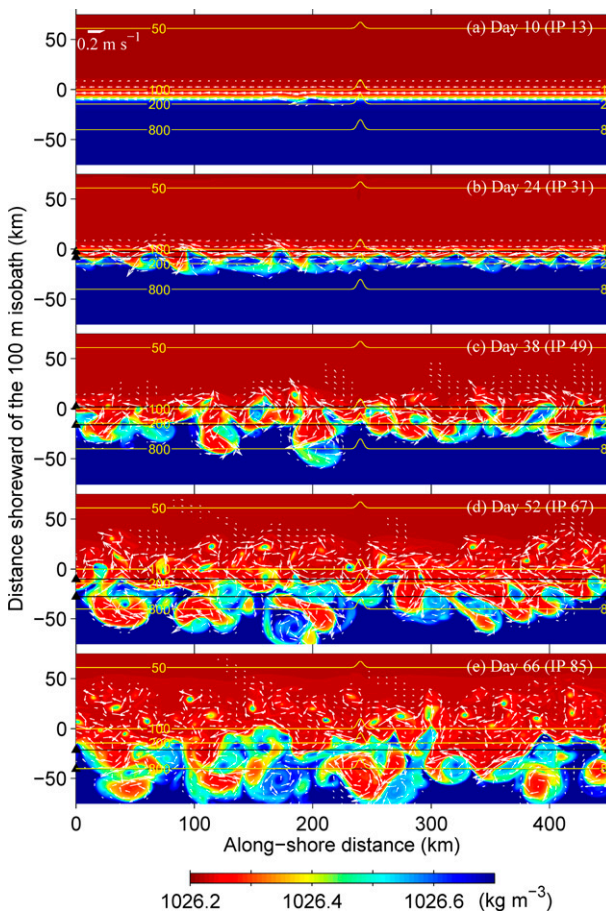

FIG. 15. Time series of density (color) and horizontal velocity (white arrows) at 10 m below surface from the simulation with one shelfbreak canyon of $l_c = 10$ km and $w_c = 5$ km. Velocity arrows with speeds of less than 0.02 m s^{-1} are omitted, and the velocity scale is given in the upper-left corner of (a). The black lines and triangles indicate the frontal perturbation zones for computing the along-shelf length scale; the yellow lines are the isobath contours. IP in the legend stands for inertial period.

which is also reflected in the variation of T_e (Fig. 16a). If the canyon topography can be treated as a type of perturbation, this influence is consistent with the aforementioned stronger initial perturbation facilitating the development of the frontal meanders. All the simulations with shelfbreak canyons show a slight increase of the perturbation length scale at the initial stage before day 40, but the trend disappears at the meander stage (Fig. 16c). The variation in λ_m is small, all within ± 5 km of that in the control simulation. These suggest that canyon topography may play a role in determining the wavelength of the fastest-growing perturbation in the initial stage but has no significant influence on the length scale of the finite-amplitude frontal meanders.

5. Summary

This study combines analytical formulation and numerical simulations to investigate the development of
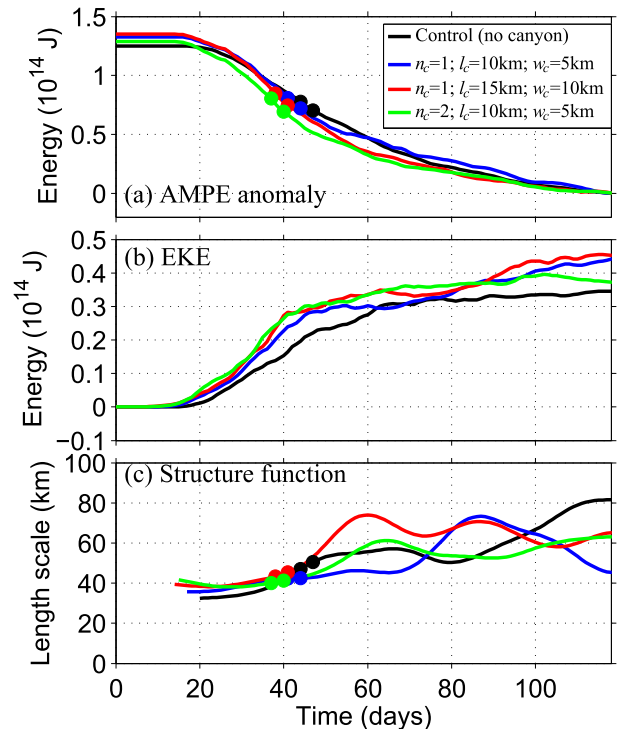

FIG. 16. As in Fig. 13, but from simulations with and without shelfbreak canyons. The legend in (a) indicates the number of canyons n_c, canyon length scale l_c, and canyon width scale w_c in each case.

the finite-amplitude meanders of retrograde shelfbreak fronts with isopycnal slope opposite to bottom slope. The system setup mimics the prominent density front at the MAB shelf break that separates lower-density shelf water from higher-density offshore waters.

Previous studies of shelfbreak fronts argued that the frontal instability is a mixture of barotropic and baroclinic instability. Numerical simulations of this study confirm this. The simulations also indicate the dominance of baroclinic instability as most of the perturbation energy is drawn from the available mean potential energy rather than mean kinetic energy. Through combining length scales of barotropic and baroclinic instability, we obtained a formula for the along-shelf length scale of finite-amplitude frontal meanders: $[b_1/(1 + a_1 S^{1/2})]NH/f$. Here, S, the Burger number measuring the ratio of the energy conversion associated with barotropic to baroclinic instability, is included to represent the influence of barotropic instability. The formulated relationships agree well with results of the numerical sensitivity simulations to a large degree, and a match of the two gives values of the empirical constants: $a_1 = 2.69$ and $b_1 = 14.65$.

We also obtained a formula for the exponential growth rate of the frontal instability during the initial stage: $[b_2(1 + a_1 S^{1/2})/(1 + a_2 \alpha S^{1/2})]NH/L$. This formula incorporates the influences of both barotropic and baroclinic instability as well as the stabilizing effect of bottom slope α (e.g., Blumsack and Gierasch 1972; Brink 2012). The formulated growth rate agrees with the results of most of the sensitivity simulations (Figs. 9f–j and 10c,d), and a match of the two gives $a_2 = 5.1 \times 10^3$ and $b_2 = 6.2 \times 10^{-2}$.

Some of the numerical simulations have initial potential vorticity $\Pi_0 < 0$ in part of the domain and show development of symmetric instability before baroclinic and barotropic instability. The modeled symmetric instability has a much smaller spatial scale and is confined within the front. Its growth leads to faster development of frontal barotropic and baroclinic instability of much larger spatial scales at later times. The simulations also suggest that the development of symmetric instability during the initial stage has no influence on the length scale of frontal meanders.

The length scale formula obtained here requires verification from observations, which can be achieved through comparing meander length scales at times of different frontal density contrast or dimensions. It also provides a framework for the investigation of the influence of large-scale forcing, for example, Gulf Stream warm-core rings, regional atmospheric heating, and upstream freshening on the MAB shelfbreak front. As warm-core rings impinge the MAB continental slope, they push the shelfbreak front onshore and squeeze the frontal zone (Chen et al. 2014b; Gawarkiewicz et al. 2001). The recently reported anomalous atmospheric heating of the MAB shelf water (Chen et al. 2014a) and increasing upstream freshwater input (Balch et al. 2012) may result in greater density differences across the shelf break. An implication of this study is that these external forcings may change the meander length scale of the shelfbreak front, modify the frontal circulation, and affect the shelfbreak exchange of heat, salt, and biogeochemistry.

APPENDIX

Notation

Table A1 provides a list of notations, their meanings, and indicates where each first appears.

TABLE A1. List of notations.

Variable	Meaning	First appearance
A	Upper 40 m of the initial frontal area	Section 3
a_1, b_1	Empirical constants	(31)–(32)
a_2, b_2	Empirical constants	(38)–(39)
C_{bt}	Energy conversion associated with barotropic instability	Section 2a
C_{bc}	Energy conversion associated with baroclinic instability	Section 2a
C_d	Coefficient of quadratic bottom drag	Section 3
c_{bt}	Coefficient representing the influence of barotropic instability	(30)
D	Vertical scale of the pycnocline	(21c)
E'	Total perturbation energy	(3)
f	Coriolis parameter	(1)
g	Gravitational acceleration	Section 2a
H	Vertical scale of the density variation of a baroclinic flow	(1)
h	Water depth and model bathymetry	(16)
h_B	Bottom elevation relative to a reference level	(5)
h_f	Shelf depth scale	(16)
h_{p1}, h_{p2}	Vertical scales of the continental slope	(16)
k_{bt}	Along-stream wavenumber for barotropic instability	(11)
k_{bc}, m_{bc}	Along- and cross-stream wavenumber for baroclinic instability	(8)
k_{si}	Along-stream wavenumber for symmetric instability	Section 2
L	Horizontal scale of the density variation of a baroclinic flow	(1)
L_s	Width of a barotropic shear flow	(11)
L_T	Cross-shelf extent of the central isopycnal of the front	Section 3
L_x, L_y	Along- and cross-shelf extent of the model domain	Section 3
L_{y0}	Cross-shelf extent of the study area within the model domain	Section 3
l_c, w_c	Canyon length scale in the cross- and along-shelf direction	(40)
l_f	Length scale of the shelf width	(16)
l_p	Cross-shelf length scale of the continental slope	(16)
$l_s(z)$	Shear zone width on the offshore side of the shelfbreak jet	Section 3
N	Buoyancy frequency	(1)
n_c	Number of shelfbreak canyons	(40)
Q	Along-shelf structure function	(24)
q	Coefficient representing the bottom-slope influence	(36)
$r_1(t)$	Time series of frontal meander length scale	Section 4a
$R_1(t)$	Smoothed time series of frontal meander length scale	Section 4a
Ri	Richardson number	(14)
Ro	Rossby number	(6)
s	Slope Burger number	(37)
S	Burger number	(1)
$[t_1, t_2]$	Time window for computing simulated perturbation growth rate	(23)
T_e	Time of AMPE reduction reaching e^{-1} of the maximum reduction in 120 days	Section 4a
(U, V)	Along-shelf (along stream) averaged horizontal velocity	(1), (22a)
(u, v, w)	Total velocity	(3)
(u', v')	Horizontal perturbation velocity	(3), (17)
(u_0, v_0, w_0)	Model initial velocity	Section 3
(u_b, v_b)	Horizontal bottom velocity in the model	Section 3
W_0	Length scale of the background cross-shelf variation	(21a)
W_1	Cross-shelf length scale determining frontal isopycnal tilt	(21a)
W_2	Cross-shelf length scale determining frontal width	(21b)
x_{ci}	x coordinate of the canyon axis	(40)
(y_0, z_0)	Reference point coordinate used in the density formulation	(21)
y_1, y_2	Cross-shelf boundaries of a baroclinic flow	Section 2a

TABLE A1. (*Continued*)

Variable	Meaning	First appearance
y_p	y coordinate of the center of the continental slope	(16)
y_{p0}	y coordinate of the center of the slope away from the canyon	(40)
α	Bottom slope at the foot of the shelfbreak front	(6)
γ	Slope of the frontal isopycnals on the seafloor	(6)
$\zeta(z)$	Vertical displacement of $\overline{\rho}(y, z)$ with respect to $\rho_d(z)$	(22b)
$\zeta'(z)$	Vertical displacement of $\rho(x, y, z)$ with respect to $\overline{\rho}(y, z)$	(22d)
η	Cross-stream displacement of a fluid parcel	(5)
η_1, η_2, η_3	Temporary variables	(21)
κ, κ_θ	Vertical turbulence viscosity and diffusivity	(18), (20)
λ_{bc}	Dominant wavelength of linear baroclinic instability	Section 2
λ_{bc0}	Scaled baroclinic instability wavelength in the control case	Section 4a
λ_{bci}	Wavelength of baroclinic instability in infinitely wide flows	(9)
λ_{bt}	Dominant wavelength of linear barotropic instability	(28)
λ_{bt0}	Scaled barotropic instability wavelength in the control case	Section 4a
λ_m	Model simulated length scale of frontal meanders	Section 4a
λ_s	Scaled length scale of frontal meanders	(30)
ξ	Sea surface height	(18)
Π	Potential vorticity	(5)
Π_0	Model initial potential vorticity	Section 4c
ρ	Potential density	Section 2
ρ'	Density perturbation relative to the along-shelf mean	Section 2
$\overline{\rho}$	Along-shelf (along stream) averaged density	(22b)
ρ_0	Reference density	Section 2
ρ_1, ρ_2	Surface density of the shelf and offshore waters	(21d)
ρ_{10}	Model density at 10 m below surface	(24)
$\rho_b(z)$	Vertical profile of density anomaly in the deep sea	(21d)
ρ_c	Density of the central isopycnal of the shelfbreak front	Section 3
$\rho_d(z)$	Vertical density profile in the deep sea	Section 3
$\Delta\rho$	Surface density difference between shelf and slope waters	Section 3
σ_{bc}	Perturbation growth rate of linear baroclinic instability	(7)
σ_{bc0}	Scaled baroclinic instability growth rate in the control case	Section 4a
σ_{bt}	Perturbation growth rate of linear barotropic instability	(10)
σ_{bt0}	Scaled barotropic instability growth rate in the control case	(10)
σ_m	Modeled perturbation growth rate of frontal instability	(23)
σ_s	Scaled perturbation growth rate of frontal instability	(36)
σ_{s0}	Scaled instability growth rate of a front on a flat bottom	(36)
σ_{si}	Perturbation growth rate of symmetric instability	(15)

REFERENCES

Allen, J. S., and P. A. Newberger, 1998: On symmetric instabilities in ocean bottom boundary layers. *J. Phys. Oceanogr.*, **28**, 1131–1151, doi:10.1175/1520-0485(1998)028<1131:OSIIOB>2.0.CO;2.

Allen, S. E., and X. Durrieu de Madron, 2009: A review of the role of submarine canyons in deep-ocean exchange with the shelf. *Ocean Sci.*, **5**, 607–620, doi:10.5194/os-5-607-2009.

Balch, W. M., D. T. Drapeau, B. C. Bowler, and T. G. Huntington, 2012: Step-changes in the physical, chemical and biological characteristics of the Gulf of Maine, as documented by the GNATS time series. *Mar. Ecol. Prog. Ser.*, **450**, 11–35, doi:10.3354/meps09555.

Barth, J. A., 1994: Short-wavelength instabilities on coastal jets and fronts. *J. Geophys. Res.*, **99**, 16 095–16 115, doi:10.1029/94JC01270.

Blumsack, S. L., and P. J. Gierasch, 1972: Mars, the effects of topography on baroclinic instability. *J. Atmos. Sci.*, **29,** 1081–1089, doi:10.1175/1520-0469(1972)029<1081:MTEOTO>2.0.CO;2.

Boccaletti, G., R. Ferrari, and B. Fox-Kemper, 2007: Mixed layer instabilities and restratification. *J. Phys. Oceanogr.*, **37**, 2228–2250, doi:10.1175/JPO3101.1.

Brearley, J. A., R. S. Pickart, H. Valdimarsson, S. Jonsson, R. W. Schmitt, and T. W. N. Haine, 2012: The east Greenland boundary current system south of Denmark Strait. *Deep-Sea Res. I*, **63**, 1–19, doi:10.1016/j.dsr.2012.01.001.

Brink, K. H., 2012: Baroclinic instability of an idealized tidal mixing front. *J. Mar. Res.*, **70**, 661–688, doi:10.1357/002224012805262716.

——, and D. A. Cherian, 2013: Instability of an idealized tidal mixing front: Symmetric instabilities and frictional effects. *J. Mar. Res.*, **71**, 425–450, doi:10.1357/002224013812587582.

Cenedese, C., and P. F. Linden, 2002: Stability of a buoyancy-driven coastal current at the shelf break. *J. Fluid Mech.*, **452**, 97–121, doi:10.1017/S0022112001006668.

Chapman, D. C., 1985: Numerical treatment of cross-shelf open boundaries in a barotropic ocean model. *J. Phys. Oceanogr.*, **15**, 1060–1075, doi:10.1175/1520-0485(1985)015<1060:NTOCSO>2.0.CO;2.

——, and S. J. Lentz, 1994: Trapping of a coastal density front by the bottom boundary layer. *J. Phys. Oceanogr.*, **24**, 1464–1479, doi:10.1175/1520-0485(1994)024<1464:TOACDF>2.0.CO;2.

Charney, J. G., and G. R. Flierl, 1981: Oceanic analogues of large-scale atmospheric motions. *Evolution of Physical Oceanography*, B. A. Warren and C. Wunsch, Eds., MIT Press, 504–548.

Chen, K., G. G. Gawarkiewicz, S. J. Lentz, and J. M. Bane, 2014a: Diagnosing the warming of the northeastern U.S. coastal ocean in 2012: A linkage between the atmospheric jet stream variability and ocean response. *J. Geophys. Res. Oceans*, **119**, 218–227, doi:10.1002/2013JC009393.

——, R. He, B. S. Powell, G. G. Gawarkiewicz, A. M. Moore, and H. G. Arango, 2014b: Data assimilative modeling investigation of Gulf Stream warm core ring interaction with continental shelf and slope circulation. *J. Geophys. Res. Oceans*, **119**, 5968–5991, doi:10.1002/2014JC009898.

Flather, R. A., 1976: A tidal model of the northwest European continental shelf. *Mem. Soc. Roy. Sci. Liege*, **10**, 141–164.

Fratantoni, P., and R. Pickart, 2003: Variability of the shelf break jet in the Middle Atlantic Bight: Internally or externally forced? *J. Geophys. Res.*, **108**, 3166, doi:10.1029/2002JC001326.

——, ——, D. Torres, and A. Scotti, 2001: Mean structure and dynamics of the shelfbreak jet in the Middle Atlantic Bight during fall and winter. *J. Phys. Oceanogr.*, **31**, 2135–2156, doi:10.1175/1520-0485(2001)031<2135:MSADOT>2.0.CO;2.

Garvine, R. W., K.-C. Wong, G. Gawarkiewicz, R. McCarthy, R. W. Houghton, and F. Aikman III, 1988: The morphology of shelfbreak eddies. *J. Geophys. Res.*, **93**, 15 593–15 607, doi:10.1029/JC093iC12p15593.

Gawarkiewicz, G. G., 1991: Linear stability models of shelfbreak fronts. *J. Phys. Oceanogr.*, **21**, 471–488, doi:10.1175/1520-0485(1991)021<0471:LSMOSF>2.0.CO;2.

——, F. Bahr, R. C. Beardsley, and K. H. Brink, 2001: Interaction of a slope eddy with the shelfbreak front in the Middle Atlantic Bight. *J. Phys. Oceanogr.*, **31**, 2783–2796, doi:10.1175/1520-0485(2001)031<2783:IOASEW>2.0.CO;2.

——, K. H. Brink, F. Bahr, R. C. Beardsley, M. Caruso, J. Lynch, and C.-S. Chiu, 2004: A large-amplitude meander of the shelfbreak front in the Middle Atlantic Bight: Observations from the Shelfbreak PRIMER Experiment. *J. Geophys. Res.*, **109**, C03006, doi:10.1029/2002JC001468.

Gill, A. E., 1982: *Atmosphere–Ocean Dynamics.* Academic Press, 662 pp.

Haine, T. W. N., and J. Marshall, 1998: Gravitational, symmetric, and baroclinic instability of the ocean mixed layer. *J. Phys. Oceanogr.*, **28**, 634–658, doi:10.1175/1520-0485(1998)028<0634:GSABIO>2.0.CO;2.

Holliday, D., and M. E. McIntyre, 1981: On potential energy density in an incompressible, stratified fluid. *J. Fluid Mech.*, **107**, 221–225, doi:10.1017/S0022112081001742.

Houghton, R. W., F. Aikman III, and H. W. Ou, 1988: Shelf-slope frontal structure and cross-shelf exchange at the New England shelfbreak. *Cont. Shelf Res.*, **8**, 687–710, doi:10.1016/0278-4343(88)90072-6.

Kang, D., and O. Fringer, 2010: On the calculation of available potential energy in internal wave fields. *J. Phys. Oceanogr.*, **40**, 2539–2545, doi:10.1175/2010JPO4497.1.

Kinder, T. H., and L. K. Coachman, 1978: The front overlaying the continental slope in the eastern Bering Sea. *J. Geophys. Res.*, **83**, 4551–4559, doi:10.1029/JC083iC09p04551.

Lamb, K. G., 2008: On the calculation of the available potential energy of an isolated perturbation in a density-stratified fluid. *J. Fluid Mech.*, **597**, 415–427, doi:10.1017/S0022112007009743.

Linder, C. A., and G. G. Gawarkiewicz, 1998: A climatology of the shelfbreak front in the Middle Atlantic Bight. *J. Geophys. Res.*, **103**, 18 405–18 423, doi:10.1029/98JC01438.

Lozier, M. S., and M. S. Reed, 2005: The influence of topography on the stability of shelfbreak fronts. *J. Phys. Oceanogr.*, **35**, 1023–1036, doi:10.1175/JPO2717.1.

Morgan, D. T., 1997: Linear instability of the shelfbreak front off the southern flank of Georges Bank. Ph.D. thesis, Dartmouth College, 190 pp.

Orlanski, I., 1976: A simple boundary condition for unbounded hyperbolic flows. *J. Comput. Phys.*, **21**, 251–269, doi:10.1016/0021-9991(76)90023-1.

Pedlosky, J., 1987: *Geophysical Fluid Dynamics.* 2nd ed. Springer-Verlag, 710 pp.

Pingree, R. D., 1979: Baroclinic eddies bordering the Celtic Sea in later summer. *J. Mar. Biol. Assoc. U. K.*, **59**, 689–698, doi:10.1017/S0025315400045677.

Shchepetkin, A. F., and J. C. McWilliams, 2008: Computational kernel algorithms for fine-scale, multiprocess, long-term oceanic simulations. *Handbook of Numerical Analysis. XIV: Computational Methods for the Atmosphere and the Ocean*, P. G. Ciarlet, R. Temam, and J. Tribbia, Eds., Elsevier, 121–183.

Stone, P. H., 1966: On non-geostrophic baroclinic stability. *J. Atmos. Sci.*, **23**, 390–400, doi:10.1175/1520-0469(1966)023<0390:ONGBS>2.0.CO;2.

Thomas, L. N., J. R. Taylor, R. Ferrari, and T. M. Joyce, 2013: Symmetric instability in the Gulf Stream. *Deep-Sea Res. II*, **91**, 96–110, doi:10.1016/j.dsr2.2013.02.025.

Todd, R. E., G. G. Gawarkiewicz, and W. B. Owens, 2013: Horizontal scales of variability over the Middle Atlantic Bight shelfbreak and continental rise from finescale observations. *J. Phys. Oceanogr.*, **43**, 222–230, doi:10.1175/JPO-D-12-099.1.

Voorhis, A. D., D. C. Webb, and R. C. Millard, 1976: Current structure and mixing in the shelf/slope water front south of New England. *J. Geophys. Res.*, **81**, 3695–3708, doi:10.1029/JC081i021p03695.

Warner, J. C., C. R. Sherwood, H. G. Arango, and R. P. Signell, 2005: Performance of four turbulence closure models implemented using a generic length scale method. *Ocean Modell.*, **8**, 81–113, doi:10.1016/j.ocemod.2003.12.003.

Zhang, W. G., G. G. Gawarkiewicz, D. J. McGillicuddy, and J. L. Wilkin, 2011: Climatological mean circulation at the New England shelf break. *J. Phys. Oceanogr.*, **41**, 1874–1893, doi:10.1175/2011JPO4604.1.

——, D. J. McGillicuddy, and G. G. Gawarkiewicz, 2013: Is biological productivity enhanced at the New England shelfbreak front? *J. Geophys. Res.*, **118**, 517–535, doi:10.1002/jgrc.20068.